Dissertation
submitted to the
Combined Faculties for the Natural Sciences and for Mathematics
of the Ruperto-Carola University of Heidelberg, Germany
for the degree of
Doctor of Natural Sciences

Put forward by:

MPhys Matthias Uljas Lutz

Born in Vienna, Austria

Oral examination: 26.07.2012

A Magnetic Force Microscopy Investigation of α-Fe, Fe_3C and Permalloy Nanowires under Applied Magnetic Fields

Referees: **Prof. Dr. Rüdiger Klingeler**
Prof. Dr. Annemarie Pucci

Kurzzusammenfassung. Diese Arbeit untersucht die Rolle der Anisotropien in nanoskaligen magnetischen Drähten. Die grundlegenden Eigenschaften sind theoretisch gut beschrieben, während reale Systeme Defekte aufweisen, welche insbesondere den Mechanismus und die Dynamik der Ummagnetisierungsprozesse beeinflussen. Für das Verständnis und die Anwendung magnetischer Nanodrähte ist daher sowohl die Kenntnis der relevanten Materialparameter als auch das Verhalten in externen Magnetfeldern von entscheidender Bedeutung. In der vorliegenden Dissertation wurde die Magnetkraftmikroskopie (MFM) in externen Magnetfeldern eingesetzt, um das remanente Verhalten und den Effekt externer Felder zu untersuchen. Eine topographische Charakterisierung erlaubt es dabei, die Morphologie eines Drahtes mit Details des magnetischen Zustandes zu korrelieren. Dabei werden zwei unterschiedliche Klassen von Nanodrähten studiert. Einerseits α-Fe und Fe_3C Nanomagnete, welche auf natürliche Weise im Inneren von Kohlenstoffnanoröhren entstehen. Zum anderen künstlich erzeugte Nanodrähte, die in Mustern angeordnet wurden, um spezielle Wechselwirkungen untersuchen zu können. Die Untersuchung der mit Kohlenstoff umhüllten Nanodrähte verdeutlicht die wichtige Rolle der Anisotropien für die auftretenden magnetischen Eigenschaften. Bei den künstlichen Nanostrukturen erzeugt die den eindomänigen Magneten auferlegte Frustration neuartige Effekte und diese Systeme können somit als Modellsystem für Quantenprozesse dienen. In beiden Fällen ist es die äußere Form der Magnete, welche die magnetischen Eigenschaften maßgeblich beeinflusst. Auch die MFM-Spitze spielt eine entscheidende Rolle, sie kann während dem Messen Schaltprozesse auslösen. Insgesamt gewähren die Ergebnisse neue Einblicke in die Physik magnetischer Nanodrähte und bieten eine Grundlage für mögliche Anwendungen.

Abstract. This thesis provides experimental insight into the role of anisotropies in magnetic wires at the nanoscale. While fundamental properties of magnetic nanowires are well described theoretically, real systems are subject to imperfections which in particular affect the mechanism and dynamics of magnetization reversal. Therefore, not only fundamental material parameters but also detailed investigations of the field dependent magnetic properties are essential before the vast potential of magnetic nanowires can be exploited. In the thesis at hand, a magnetic force microscope (MFM) with internal magnetic fields was employed to study the remanent behavior of the nanowires and the effects of applied fields. A physical characterization allows one to connect the morphology of the wire to its magnetic response. The magnetic characteristics of two types of nanowires are studied. Firstly, α-Fe and Fe_3C nanowires naturally formed within multiwalled carbon nanotubes. Secondly, tailored nanowires arranged in patterns causing well defined interactions. For the carbon coated nanowires, the results highlight the importance of anisotropies in deciding the behavior of magnetic nanowires. For the artificial nanostructures, frustration imposed on the single domain magnets yields novel effects highlighting that the wires can be used as a model system for quantum processes. In both cases the shape, either imposed by the rigid cage of a carbon nanotube or tailored to ones specifications, is crucial in the context of the magnetic properties. Also the MFM tip itself plays a deciding role as it can cause switching in the magnet it is measuring. The results give new insight into the physics of magnetic nanowires and lay the groundwork for potential applications.

Für Alice

List of Abbreviations

AFM	Atomic Force Microscope/Microscopy
BSED	Back Scattered Electron Detector
CNT	Carbon Nanotube
CVD	Chemical Vapor Deposition
EBL	Electron Beam Lithography
EFM	Electrostatic Force Microscope/Microscopy
GS	Ground State
HEC	High Energy Configuration
hr-MFM	High Resolution MFM
IFO	In-Plane Field Option
MCA	Magneto Crystalline Anisotropy
MFM	Magnetic Force Microscope/Microscopy
PFO	Perpendicular Field Option
SA	Shape Anisotropy
SEM	Scanning Electron Microscope/Microscopy
TEM	Transmission Electron Microscope/Microscopy
TLD	Two Lens Detector

Contents

Introduction

Manipulating the properties of matter via their scale is a fascinating approach to expand the horizon of knowledge and technology. New effects emerge at the nanoscale, the physics of which have to be studied so as to allow them to be harnessed for real life applications. By reducing the dimensions of a magnet a new magnetization state becomes accessible: the single domain arrangement which always emits a stray field. To be precise, a single domain magnet is here defined with all moments being parallel, because in theory a magnetic circle can contain the entire flux, but each moment would be at a slightly different angle.

As the title of this thesis indicates, the main focus lies on the investigation of magnetic nanowires with the magnetic force microscope (MFM). The theories behind the magnetization behavior of nanowires are well established but still lacking when applied to real nanomagnets. This is mainly due to structural imperfections leading to nucleation sites which reduce the theoretical switching field. Magnetic nanowires are a fascinating subject for research. Domain walls are proposed as a means of efficiently storing and quickly accessing data (racetrack) [1] and single domain wires are employed for logic devices [2] and to simulate Ising spins in systems such as artificial spin ice [3] or to remotely treat cancer by applying heat [4].

New materials often emerge in the wake of other discoveries, as is the case with the nanowires encapsulated by carbon nanotubes (CNT). The CNT acts as a cage which not only imposes the shape for the wire but also ensures its chemical inertness and a certain degree of physical protection. CNTs are supramolecular nanostructures which can be described as rolled up sheets of graphene capped with half of a fullerene. A single walled carbon nanotube (SWNT) consists of one layer, while a multi walled carbon nanotube (MWNT) is made up of two or more concentric shells. Since only MWNT are treated they will be simply referred to as CNT henceforth. Due to the strong sp^2 carbon bonds and their regular structure CNT feature outstanding mechanical properties, very high chemical stability, intriguing electronic properties and bio-compatibility. In the context of this thesis the most interesting property is their very high stiffness, imposing a rigid cage for the filling which is thought to play a decisive role in the formation and morphology of the encapsulated nanowires.

The two cases discussed in this thesis, α-Fe and Fe_3C (iron carbide) filled CNT, highlight the importance of the surrounding nanotube. Especially for iron carbide this is the case, which is metastable at room temperature and pressure, but has remained in its single crystal cementite form practically indefinitely when enclosed by a CNT. The magnetization of the two materials is determined by the competition between the magnetocrystalline anisotropy (MCA) and the shape anisotropy (SA), resulting in different remanent magnetizations. For α-Fe the shape anisotropy dominates and forces the remanent magnetization along the long wire axis, while for iron carbide the MCA is stronger and forces the magnetization along the c-axis which is oriented perpendicular to the long axis for all wires studied. The combination of stabilizing the iron carbide crystal and forcing its magnetization into a transverse arrangement opens the door for future investigations into possible applications. High anisotropy magnets are of vital importance for electromotive and renewable energy applications, being essential components of electric motors and generators.

Studying the fundamental properties of magnetic nanowires and relating them to their morphology sparks the desire to do the opposite: manipulate magnetic properties by tailoring the nanowires. Such artificial nanowires can be arranged into frustrated arrays simulating environments encountered in certain crystals. The concept of spin-ice gained a lot of attention by producing effective magnetic monopoles [5]. The single domain magnetic nanowires are here employed to simulate Ising spins, based on the fact that they have a bistable magnetization state, a property which depends on the strength of the effective anisotropy.

The centerpiece of this investigation is the magnetic force microscope (MFM) which maps the influence of the sample stray field on a driven cantilever terminated by a magnetic tip. This instrument allows one to assign directions to the magnetization vectors of the nanowires and measure the switching field by applying an external magnetic field. The influence of the magnetic tip on the magnetization state of the sample can be a nuisance, but it should also be possible to purposefully harness it. The MFM with which most of the measurements were conducted features the possibility to apply magnetic fields, either perpendicular to or in the sample plane. Applying fields allows one to measure the switching field of the nanomagnets as well as switch individual elements which in principle would reveal the underlying microscopic mechanism. This could be achieved by bringing an object close to switching by the external field, and then using the tip field to nudge a selected structure over the energy barrier.

The intricacies of nanomagnetism are explored in chapter 2 (**Theoretical Background**) along with other relevant concepts. The methods employed to achieve the aims outlined in this introduction are presented in chapter 3 (**Methodology**). The results and discussion for the nanowires encapsulated in carbon nanotubes are presented in chapter 4 (**Results and Discussion I**), those for tailored nanowires in chapter 5 (**Results and Discussion II**) which also contains a final comparison of all studied nanowires and the conclusions. This thesis is rounded up by a brief **Summary**.

Theoretical Background

This chapter aims at laying the groundwork for understanding the observations and discussion thereof presented in this thesis. A brief introduction into carbon nanotubes will be followed by the main part concentrating on magnetism, especially ferromagnets with a focus on nanoparticles. The case of nanomagnets is a special one, often the characteristic lengths are of the same order as the particle size, giving rise to novel phenomena not experienced in bulk samples. The final section will discuss the physics motivating the research into artificial patterns of deposited nanowires. The theoretical concepts behind magnetic force microscopy and chemical vapor deposition will be discussed in the next chapter, hand in hand with the description of the apparatus and experimental procedures.

2.1 Carbon Nanotubes

In retrospect the 'discovery' of carbon nanotubes (CNT) was claimed by various groups, who had found such structures but did not cause such an impact as Ijima did with his description of 'needles' consisting of concentric 'tubes' [6]. CNTs have drawn a lot of attention due to their mechanical and chemical stability as well as their electronic [7] and optical [8] properties. The origin of those special properties is the resemblance to graphene which has hence eclipsed CNTs in attention. Graphene is a single layer of graphite, consisting of a planar lattice of triple bonding carbon atoms. The four valence electrons of carbon (two 1s and two 2p electrons) hybridize to form three sp^2 σ-bonds. Theses three bonds lie in a plane, separated by 120°, while the fourth electron (p) is in a free π orbital pointing out of the plane. A CNT can be seen as a sheet of graphene rolled up on itself. A half fullerene of the appropriate size usually caps the end of such a single walled nanotube (SWNT). It is important to mention that CNTs do not actually form in this manner (see below for growth process) but it is convenient to describe them as rolling up a sheet of graphene. The way the sheet is rolled up relative to the bond angels decides the electronic and optical properties of the SWNT. Often multiple nanotubes are formed as concentric shells, with a fixed spacing of 0.34 nm between the layers. Such a structure is called a multi walled carbon nanotube (MWNT), sometimes specified as double walled (DWNT) where relevant. The structures encountered in this thesis are all MWNT, and the property most relevant to this thesis is their stiffness and stability.

The maximum measured value for Young's modulus is 950 GPa [9] and for tensile strength 150 GPa [10]. Experiments on the radial stiffness, by external compression, revealed that empty tubes are rather easy to compress [11]. Experiments to test their resistance to an expansion of the filling would be hard to realize for technical reasons. Expansion for a single tube could be modeled by considering an according increase in diameter, and hence involve the in plane elastic modulus. Since multiple layers are involved this would prove an exercise beyond the scope of this thesis. Considering the fact that multiple walls are present and that the iron fills out the entire inner diameter of the innermost tube it stands to reason that not much if any deformation will take place. The CNT themselves are diamagnetic and hence do not actively contribute to the magnetic properties of the filling [12]. The iron filling mentioned above is the actual focus of this thesis, since at this length scale it behaves as a single domain magnet.

2.2 Magnetism

The magnetic properties of nanoparticles are described by a series of fundamental concepts which will be elaborated in this chapter. This thesis only deals with ferromagnetic particles below the single domain limit, a very special niche between classical domain based magnetic properties and the superparamagnetic behavior of very small or soft particles. Domain walls do come into play when applying magnetic fields, playing a role in magnetization switching mechanisms, and at the interface of exchange coupled single domain particles in artificial arrangements. The fundamentals of magnetism will be elaborated, focusing on anisotropies.

2.2.1 History and Origin of Magnetism

One of the first references to magnetism is given by the Greek philosopher Thales of Miletus in the 6th century BC [13]. The mineral he describes consists of a mixture of two iron oxides, Fe_3O_4 (magnetite) and Fe_2O_3 (maghemite), and is commonly referred to as loadstone. It is the only magnetized material found in nature, which is probably magnetized during a lightning strike [14]. It was used early on in history by the Chinese for aligning architectural elements according to Feng Shui and globally for navigation. The compass is one of the earliest applications and one that most people understand. A needle magnetized along the long axis will try to align itself with the ambient magnetic field, and therefore always points toward the earths magnetic poles in the absence of other fields. The ancient Greek word "Ferro", referring to the element uron is the namesake for the best known type of magnetism. Iron is the typical ferromagnet, the varying properties of different allotropes and composites are of great importance and relevance to this thesis and will be discussed in detail. The distinguishing property of a ferromagnet is that it is magnetized even in the absence of a magnetic field.

Magnetic charges always come in opposite pairs. This property is also strongly related to the comparison to angular momentum, since a rotating object always has two 'poles' at the ends of the axis of rotation. Magnetism and electricity are closely interconnected, a relationship summed up by Maxwell's equations.

Amperes circuit law with Maxwell's correction

$$\nabla \times B = \mu_0 J + \mu_0 \epsilon_0 \frac{\partial E}{\partial t} \tag{2.1}$$

shows how both an electric current (density) J as well as a changing electric field E cause a magnetic flux density B. μ_0 is the permeability and the ϵ_0 the permittivity of vacuum. Solid state magnetism is of atomic origin, governed by quantum phenomena. The nucleus and electrons can be seen as moving/rotating charges, which cause a magnetic moment according to Equation 2.1. The nucleus of an atom has a very weak moment, exploited in techniques such as nuclear magnetic resonance. The main source of magnetic moment are electrons in partially filled electron shells. The larger part of an atom's magnetic moment comes from the electron spin, a property equivalent to the classical angular momentum. Magnetic moment is measured in units of Bohr magnetons, defined as μ_B = e$\hbar/2m_e$ with the value 9.2740*10^{-24} J/T.

The following description of magnetism is based on the arguments of Myers [15]. The atoms of all elements are magnetic, the presence of an external magnetic field induces a magnetic dipole moment. A subset of atoms possesses a permanent magnetic moment, an even smaller subset of which still exists in the solid state. These three sets are diamagnetic, paramagnetic and ferromagnetic materials respectively. The classification of magnetic matter is best described by the magnetic susceptibility χ, a quantity which is also easy to measure experimentally. It is given by

$$\chi = \mu_0 \frac{M}{B_0} \tag{2.2}$$

where M is the magnetic dipole moment per unit mass and B_0 is the external magnetic field.

The most general case is that of **Diamagnetism**, an effect which is always present in matter. An external magnetic field influences the electron orbitals. Treating an orbiting electron like a resistance less current loop one can apply Lenz's law, which states that a field is formed opposing the external one. The susceptibility is therefore negative, a result of the induced dipole moment. The diamagnetic effect is always weak and only significant when no other forms of magnetism arise, in which case it is treated as a correction factor.

A simple picture of **Paramagnetism** is that non-interacting moments, oriented randomly and therefore seemingly unmagnetized, align parallel to an external applied field in turn causing a magnetic field. For atoms this would mean that in an external magnetic field, electrons will move to higher energy orbitals to align their spins parallel with the field. This leads to a positive susceptibility. Upon removing the external field the order is destroyed by thermal fluctuations.

A full shell has no resultant spin or orbital angular momentum and therefore no inherent magnetic moment. These elements or ions show a diamagnetic response as described above. As soon as a shell is only partially filled a permanent magnetic moment arises. Therefore most atoms (and ions) have an associated atomic magnetic moment when they are in isolation. As soon as they form inter atomic bonds, the majority of atoms looses its magnetic moment. In most cases the reason is that bonds between atoms form by exchanging or sharing electrons, thereby creating effectively filled shells. In the solid state there are two cases where paramagnetism is preserved: in certain aggregates of non-interacting magnetic atoms (found in magnetic salts) and Pauli spin paramagnetism in some band metals. Band magnetism will be further discussed below.

When atoms come close enough for the electrons to interact (< 1nm), one has to consider the exchange interaction which is defined below. In a crystal the neighbor effects governed by the exchange interaction can be summed up by the so called molecular field, which is responsible for long range magnetic order. Depending on the bond geometry and crystal composition this effect leads to ferromagnetism, antiferromagnetism and ferrimagnetism. The materials examined in this thesis are all ferromagnetic, therefore the primary focus of the theory section will lie on this aspect.

2.2.2 Ferromagnetism

Ferromagnetic matter features a permanent magnetic moment, stable up to the curie temperature T_C at which the thermal excitations of the electrons overcome the exchange interaction.

The following description is based on the arguments of Chikazumi [16]. Heisenberg postulated the exchange interaction to explain the strength of the molecular field. A simple picture can be drawn by considering two atoms with an unpaired electron each. Due to the Pauli exclusion principal a common orbit can only be established for electrons with opposite spins, allowing the atoms to come closer together thereby increasing the electrostatic Coulomb energy. Parallel spins on the other hand force the electrons into different orbitals, keeping the atoms further apart and hence saving Coulomb energy. The Coulomb energy saved is orders of magnitude larger than the magnetic dipole interaction energy of the two parallel spins thus favoring such an arrangement.

A simple exression for the direct interatomic exchange is given by:

$$E_{ex} = -2J\mathbf{S_i} \cdot \mathbf{S_j} \tag{2.3}$$

The magnetization is at a maximum at 0K and decreases slowly initially, then very abruptly before the Curie temperature. Above T_C, ferromagnetic matter behaves paramagnetically, the temperature dependence of the susceptibility is described by the Curie-Weiss law

$$\chi = \frac{C}{T - T_C} \tag{2.4}$$

where C is the Curie constant and T the temperature.

To explain the reason for the spontaneous magnetization of ferromagnetic materials, Weiss employs an inner magnetic field, given by λM, to give the effective field B_e.

$$B_e = B_0 + \lambda M \tag{2.5}$$

The main argument of this simple picture is that a small fluctuation in an initially demagnetized material causes a δM which in turn causes a δB_e through Equation 2.5, magnetizing the rest of the material.

A more complete picture is obtained when considering the atomic moments. They can be estimated from the low temperature saturation magnetization. Isolated atoms have, by definition, moments which are integer values of μ_B, while experimental values for all ferromagnetic materials reveal non integer values. This fact can be explained by the concept of **band magnetism**. In the case of transition metals, the d-band is split into a spin-up and a spin-down sub-band, one of which has a slightly higher energy than the other depending on which is parallel to the external field. If the split is precisely at the Fermi energy, the low energy band is full while the high energy band remains partially empty. This causes a net spin per atom, not confined to integer values. The exchange interaction favors parallel spins which costs kinetic energy since the electrons are then required to have different k vectors. If the density of states is high, there is only a small increase in kinetic energy for an electron transfered from the low to the high energy band. If the exchange energy saved is greater than this cost then a stable ferromagnetic state forms. The picture of band magnetism is not complete, one of its main flaws is the failure to explain the Curie-Weiss like behavior above T_C which would indicate local atomic moments. A further point is that in pure band magnetism there would be no spin-orbit interaction. This would result in an absence of magnetocrystalline anisotropy (discussed in detail later) which is not observed.

2.2.3 Domains

According to what was discussed about magnetism so far, objects consisting of ferromagnetic matter should be permanently magnetized. As known from daily life this is not the case, iron for example only becomes magnetized in the presence of a magnetic field. The solution to this puzzle was delivered in 1907 by Weiss. His explanation is that an object consisting of a ferromagnetic material seems unmagnetized because it separates into regions with different magnetization directions, causing the average magnetization to be zero. An applied magnetic field of sufficient magnitude will cause the entire sample to become magnetized parallel to the field. The strength of the field required to achieve this is called the saturation field. Starting from the demagnetized state the 'virgin curve' is followed until the magnetization increases to saturation, where all moments are parallel to the external field. Upon reducing the external field, the magnetization remains at saturation since it would cost exchange energy for the moments to deviate from the internal field. At a certain point the energy gain by reducing the stray field outweighs the cost of exchange energy, and the magnetization starts to decrease. The reduced magnetization at zero applied field is called remanence. When a field in the opposite direction is applied the old arrangement becomes more and more unfavorable. The negative field required to effectively demagnetize the sample is called coercive field, at this stage one could in theory reduce the negative field back to zero, at which point the sample should be demagnetized. Since the curve has a high gradient around this point there is usually some residual magnetization. The curve is then mirrored in the negative field. Now returning to positive saturation, the magnetization does not pass through the origin and follow the 'virgin curve' but instead mirrors the path taken to negative field, upon reaching positive saturation the hysteresis loop is closed. The name comes from the fact the magnetization arrangement at given field depends on whether one is starting from the demagnetized state, positive or negative saturation or an incomplete magnetization, in other words: the history of the sample. To demagnetize a sample one can alternatingly magnetize the sample in decreasing positive and negative fields, but a real return to the virgin state is only achieved by heating the sample above T_C. The incomplete magnetization mentioned above leads to minor loops which are important factors when discussing soft magnetic materials.

Soft Materials are those where the magnetization process encounters little opposition and the hysteresis loop is very tight. Such materials have applications where hysteresis and the accompanied energy loss are a hindrance, as for example in transformers where the continuous switching would cause a lot of heat loss. The opposition mentioned above comes in the form pinning sites for domain walls, which stop the domains from expanding throughout the sample, and magnetocrystalline anisotropy (MCA) which causes an additional energy cost for the magnetization of a domain to rotate so as to align the moments with the external field. The more and efficient pinning sites and/or higher the MCA the harder a bulk ferromagnet, and the more boxlike the hysteresis curve becomes.

The extreme case is a high anisotropy single domain particle which has a perfectly square hysteresis loop. The special case of single domain magnetism is the main focus of this thesis. To understand the influence of the two main anisotropy contributions treated in this thesis, their physical origin has to be explored.

2.2.4 Shape Anisotropy

Shape anisotropy (SA) is a consequence of magnetic surface charges which arises when a stray field emanates from a magnet. The following descriptions is based on the arguments by Skomski [17]. SA is a magnetostatic effect which is very important at the nanoscale, especially when considering very anisotropic structures such as wires or thin films. In an otherwise isotropic single domain particle, a deviation from spherical shape causes nonzero energy difference for different macroscopic magnetization directions. This is caused by the stray field, which seeks to minimize. The magneto static energy E_{ms} of an ellipsoid is given by

$$E_{ms} = \frac{\mu_0}{2} M_s^2 (D_x s_x^2 + D_y s_y^2 + D_z s_z^2) V \tag{2.6}$$

where V is the volume and x, y and z the principal axes of the ellipsoid with corresponding demagnetizing factors D_i and directional cosines s_i. Specifying the case for an ellipsoid of revolution (the case relevant for wires), where $D_x = D_y$ and $D_x + D_y + D_z = 1$ leads to an expression for the shape anisotropy factor K_{sh}.

$$K_{sh} = \frac{\mu_0}{4} (1 - 3D_z) M_s^2 \tag{2.7}$$

For infinite wires D_z converges to zero further simplifying equation 2.7.

2.2.5 Magnetocrystalline Anisotropy

As the name suggests, (MCA) is a consequence of the crystal structure of the ferromagnet. The influence of the crystal orientation on the preferred magnetization direction is caused by **Spin-Orbit coupling**. A simple picture explaining this phenomenon is that the partially unoccupied 3d orbitals are influenced by the electrons forming bonds to the neighboring atoms. One can see this as the dipole interaction between the field caused by an electron's orbital motion and its spin moment. In a free atom 3d wave functions can be seen as circular currents traveling in their respective orbitals. This gives rise to orbital moments.

Combined to a solid, the electrostatic crystal field usually quenches the orbital moment of the electrons by forcing them into standing waves. This effect is combated by spin-orbit coupling, which results in a small induced orbital moment. This concept is crucial for understanding the magnetic properties of nanowires which often consist of a single crystal. The basic picture of MCA is that due to the electrons locked in bonds with the neighboring atoms, some directions cost more energy for the orbitals of the 'free ones' than others. To justify this one has to move a way from the pure band magnetism picture and consider localized effects. The electrons responsible for magnetism are not freely moving in the band but still feel localized effects and interact with the bonded electrons which allows spin-orbit coupling to impose an energy landscape. This leads to MCA. In the d-band magnets such as iron the induced orbital moment is small, that is why the cubic α-Fe has a very low MCA. The case gets more complicated when reducing the symmetry of the crystal, for example Fe_3C is orthorhombic and posses a strong MCA, although still small when compared to the 4f magnets whose unpaired electrons are very close to the nucleus and hence are dominated by local behavior.

For low symmetry crystals the anisotropy energy density is given by

$$\frac{E_a}{V} = K_1 V sin^2\theta + K_1' sin^2\theta cos(2\psi) \tag{2.8}$$

with K_1 the anisotropy constants, V the volume of the magnet and θ and ψ the magnetization angles relative to the easy axis. Spin-orbit coupling can be described by

$$\hat{H}_{SO} = \lambda(L \bullet S) \tag{2.9}$$

L is the orbital moment operator, S the spin operator and λ the spin-orbit coupling constant.

3d magnetism originates mainly from the spins, but the spin-orbit interaction requires an orbital moment. This is explained by the orthogonal nature of the 3d wave functions. Orthogonal superpositions of those can yield the same mathematical results but have different underlying physics.

The final statement is that the spin moment of an electron forces an orbital moment over the crystal field induced quenching, thus the strength of the MCA depends on the magnitude of the electron orbital moment which depends on the spin-orbit coupling.

The 3d magnetism encountered in the nanowires studied in this thesis generally has a low MCA, as seen for α-Fe. The 4f magnetism of the rare-earths is typically an order of magnitude larger. An interesting case is Fe_3C, which exhibits a noticeable MCA despite the origin of magnetism being 3d electrons (discussed in detail below).

2.2.6 The Single Domain Limit

The notion of a single domain magnet is essential for the concepts treated in this thesis. With decreasing size, a domain wall occupies an increasing fraction of the volume of a particle, with the associated energy cost becoming dominant. At a certain size the cost of a stray field falls below that of maintaining a domain wall or vortex state, and the particle will be completely magnetized in one direction. This magnetization arrangement does not have to be uniform throughout, certain edge effects are expected. This energy trade off leads to the idea of a critical diameter D_{cr}, for spheres this is given by

$$D_{cr} = \frac{72\sqrt{AK}}{\mu M_s^2} \tag{2.10}$$

which is of crucial importance for classifying superparamagentic particles. A is the exchange stiffness, K the MCA constant and M_s the saturation magnetization of the according the material.

Crucial here is the domain wall energy density given by

$$\gamma_w = 4\sqrt{AK} \tag{2.11}$$

For inhomogeneous forms the picture gets more involved, since now also the magnetostatic effect of shape anisotropy comes into play. For prolate structures this means that the magnetization will always tend to be along the longest axis, meaning that a domain wall would either have to form along the entire length of the particle, or be head-to-head. Both options are very expensive in terms of energy. Considering a sphere below the D$_{cr}$ and stretching it along one axis, the resulting needle will retain its single domain ground state.

The case of an imposed transverse magnetization, as is the case with iron carbide, requires special attention. From a graph found in [18] the following relation is derived for the single domain limit

$$\frac{LK_d}{0.4\gamma_w} > x^{0.9} \tag{2.12}$$

where L is the length of the wire, x the aspect ratio and K$_d$ the shape anisotropy constant ($= \frac{J_s^2}{2\mu_0}$) and γ_w the domain wall energy. Entering the numbers for a 400nm long and 8nm diameter iron carbide nanowire: ($J_s = 1.23T, A = 8.7 * 10^{-12} Jm^{-1}$ and $K = 394 * 10^3 Jm^{-3}$ we get $150 > 33.8$ which is true.

2.2.7 Mechanisms of Magnetization Reversal

This section closely follows the arguments of Skomski [17]. The main types of magnetization reversal mechanism for a single domain particle are coherent rotation, curling mode and domain wall based mechanisms. They are based on different theoretical concepts and are clearly distinguishable from their angular dependence of the switching field.

Coherent rotation is the most straightforward of the mechanisms. The spins remain exchange coupled at all time, rotating simultaneously and parallel to each other in the same plane. The energy barrier in this case stems from the effective anisotropy, since a deviation from the easy axis costs energy. For an ellipsoid of rotation with unixial anisotropy the angular dependence of the switching field can be described by the so called Stoner-Wohlfarth astroid. The most noticeable feature is the 90° symmetry. The switching field applied parallel to the anisotropy axis for coherent rotation (H_{coh}) of an infinite wire is given by

$$H_{coh} = \frac{2K}{\mu_0 M_s} + \frac{M_s}{2} \tag{2.13}$$

where K is the unixial anisotropy constant and M$_s$ the saturation magnetization of the material. It is important to notice that it is independent of the size of the particle. Measured values rarely approach this theoretical value, since in most real object reversal is nucleated at a structural imperfection.

Above a certain radius it becomes energetically favorable to break the exchange coupling to save stray field energy. The mechanism classically pitted against coherent rotations is the **curling** mode, where the moments reverse by rotating in a chiral fashion around the central axis, costing them exchange energy by no longer being parallel to each other but saving stray field energy. The switching field by the curling mechanism for an infinite wire with uniaxial anisotropy K for a field applied parallel to the long axis is given by

$$H_{cur} = \frac{2K}{\mu_0 M_s} + \frac{6.78A}{\mu_0 M_s R^2} \tag{2.14}$$

This can theoretically be directly compared to coherent rotation, making it easy to distinguish the two due to the 180° symmetry of curling mode.

The curling mode is the easier path to reversal, but requires a minimum diameter to work. This critical diameter as border between coherent and curling mode as relevant reversal mechanism is defined by

$$D_{cr}^{rev} = 5.2 l_{ex} \tag{2.15}$$

where l_{ex} is the so called exchange length given by

$$l_{ex} = \sqrt{\frac{2A}{\mu_0 M_s^2}} \tag{2.16}$$

The final mechanism features a domain wall which is formed at one end and propagates through the sample. This can occur despite the wire being under the single domain limit, since it is a non-equilibrium process. For this mechanism the domain wall has to be nucleated either at a structural imperfection, or the external field is not homogeneous over the entire wire. This nucleation process is often in the form of a curling event, the reason why the two often share the same 180° symmetry [19]. To specify: a small volume undergoes magnetization reversal, which then expands by a domain wall.

2.2.8 Magnetism of α-Fe, Fe_3C and Permalloy Nanowires

The main difference between the three materials relevant to the work presented in thesis is the magnitude of their MCA.

The most common form of iron is α-Fe, which has a body centered cubic (bcc) crystal structure. It is classified as a soft magnet due to its low MCA of 0.048MJ/m^3. This weak MCA has a cubic symmetry, the easy axis being along the edges of the unit cell. It has a high saturation magnetization of 2.15T and a Curie temperature of 1043K.

Fe_3C is one of several iron carbides, known as cementite. It is metastable at room temperature and pressure and is usually classed as a ceramic due to its brittleness. Under ambient conditions it is metallic and orders ferromagnetically. It has a high spin ground state and an excited low spin state, giving Fe_3C Invar properties. Twelve iron and four Carbon atoms form an orthorhombic unit cell, where a distinction has to be made between the four iron atoms at site Fe_1 and those at the site Fe_2. They feature magnetic moments of 1.98 μ_B and 1.74 μ_B respectively [20] as calculated by Häglund et al. using the linear-muffin-tin-orbital approach. Arzhnikov et al., using first principal density functional theory, calculated 2.01 μ_B and 1.94 μ_B [21] respectively. Experimental (average) values are quoted as 1.72-1.78 μ_B [22] and 1.78 μ_B [23]. This accounts for the fact that the saturation magnetization M_s is reduced to 1.23 Tesla. A Curie temperature of 216°C allows one to estimate the exchange energy E_{exch} as 5.49*10^{7}Jm^{-3} [21], leading to an exchange constant of A_{ex} 8.7*10^{-12}. The electronic structure of

Fe_3C reveals that a hybridization between the Carbon 2p sates and iron 3d states takes place (below the Fermi level) resulting in a Fe valence electron concentration of 8.67 [24]. Further, the Fe 3d states are very asymmetric, indicating a strong local character for the magnetic moments [25]. This local character and the orthogonal lattice (a = 4.526Å , b = 5.087Å, c = 6.744Å) account for the high MCA of Fe_3C, measured by Blum and Pauthenet [26] and calculated by Arzhnikov [21]. The author will be working with the room temperature experimental value ($3.94*10^5 Jm^3$) which is the energy cost for the magnetization to be along the hard b-axis as compared to the easy c-axis. The cost for the mid-hard a-axis relative to the easy c-axis is $1.18*10^5$ Jm^3

Permalloy was specifically designed to possess close to zero MCA, making it the model soft magnet as required for transformer applications. This property also makes it ideal for tailored nanowires, since the orientation of crystal axes relative to 'cut out' wires is irrelevant. It consists of roughly 20% iron and 80% nickel. It has a saturation magnetization of 1T and a Curie temperature of 850K.

The most relevant properties of the three materials are summarized in Table 2.1 below.

material	μ M_s (T)	K_{sh} $(J/m^3)*10^5$	K_{MCA} $(J/m^3)*10^5$
Permalloy	1.00	2.0	0.05
α-Fe	2.15	9.2	0.48
Fe_3C	1.23	3.0	3.94

Table 2.1: Summary of relevant values for the three materials encountered in this thesis.

2.3 Patterned Elements

The many advantages of having nanowires within a carbon nanotube are met with one major disadvantage: one has to work with what is found, thus no precise control over wire diameter and length is possible. Further, it would be a very tedious task to purposefully arrange such wires into geometries to study their interactions. One of the strengths of nanowires with high uniaxial anisotropy is their resemblance to individual spins. The magnetization has two stable states along the axis with an energy barrier in between. Further, dipolar interaction of the single domain magnets mimics the properties of individual electrons, preferring antiparallel arrangement. This allows one to create nanoscale logic elements, store data and with the aid of geometries causing frustration one can simulate a novel class of materials: spin-ice.

2.3.1 Spin-ice

Spin-ice [27] is a term used to describe a certain class of geometrically frustrated magnetic crystals with magnetic moment μ_i located at the sites i of the lattice. The crystal has a pyrochlore structure, the magnetic ions are arranged in corner sharing tetrahedra [28]. These moments behave like Ising spins where $\mu_i = \mu S_i$ e_i with $S_i = \pm 1$ and $\mu = |\mu_i|$. The ground state of such a system is compared to the proton arrangement in solid $H_2 0$, hence the term 'ice'. Similar to water-ice, spin-ice also has a residual low temperature entropy. This class of materials has gained attention recently due to the occurrence of so called 'magnetic monopoles'. This does not imply that Gauss' law $\nabla \cdot B = 0$ is no longer valid, since these are not elementary particles but effective sources and drains of flux, connected by Dirac strings [29]. The 'ice-rules' state that in the ground state always two spins point in and two out of a junction. Excitations can violate the 'ice-rules', creating a pair of effective monopoles which are mobile and tend to drift apart.

In 2004 experiments conducted by Aoki et al. [30] and Higashinaka et al. [31] on the spin ice $Dy_2Ti_2O_7$ revealed a strange phase transition. Castelnovo and coworkers [5] show evidence that the formation of effective monopoles can explain this phase transition.

The artificial lattices created for the MFM studies presented in **Results II** have their own set of 'ice-rules', establishing a theoretical set of conditions for the ground state arrangement of such systems. For isolated single domain magnets they act to minimize dipole interaction, while for the exchange coupled ones, as employed here, they also minimize the stray field emanating from the intersections. The two types of lattice simulated here are the honeycomb lattice and a square lattice. Each single domain wire contributes a +1 and a -1 at the respective poles. The honeycomb lattice is made up of triple junctions, resulting in a stray field emanating from the intersection. The resultant stray field at the junctions can be seen as a magnetic charge of integer value, and will hence forth be referred to as such. The ground state arrangement for triple junctions is either 2in1out or 1in2out, referring to the arrows used to represent the vectors of the magnetization direction. Those two arrangements result in a net magnetic charge of +1 and -1 respectively at the intersection. The excited state would be ± 3, with all wire magnetizations pointing in or out (3in/3out). For the quadratic lattice there exists a charge neutral ground state, 2in2out. Two excited states exist, 1in3out/3in1out with charge ±2 and 4in/4out with charge ±4. With the focus lying on edge effects, further possibilities arise. In the hexagons there are 120° double junctions at the edges with a possible 1in1out (0) ground state and a 2in/2out excited state (± 2). For the square lattice one also has to consider T-shaped triple junctions at the edges, and 90° double junctions at the corners with the same possible charges as mentioned above. All these integer charge states should be clearly distinguishable under the magnetic force microscopy (MFM).

The respective excited states, can be seen as 'magnetic monopoles' comparable to the ones mentioned above, since in theory it can exist without a designated local counterpart of the opposite magnetic charge.

To study the influence of the effects described in this chapter and fulfill the the aims outlined in the Introduction one requires a set of tools to produce and study the nanowires in question, discussed in the next chapter (**Methodology**).

Methodology

This chapter focuses on the tools and methods employed for the work described in this thesis. The main focus will be on magnetic force microscopy (MFM), the tool at the center of this investigation. Scanning electron microscopy (SEM) and transmission electron microscopy (TEM) are briefly explained, focusing on the technical details relevant to this thesis. An understanding of the production of the nanowires by chemical vapor deposition (CVD) and an electron beam lithography/metal deposition process is crucial. The steps necessary to prepare samples for the investigations and a brief description of the measurement procedure are the last part of this chapter, leading into the results and discussion of the next chapter.

3.1 Microscopy

The central tool for the experimental work for this thesis is the MFM. It visualizes magnetic stray fields which allows one to assign a direction to the magnetization vectors of the corresponding nanomagnet. In this work no quantitative information about a samples stray field is determined, since the qualitative picture is sufficient to determine the magnetization arrangement of nanowires. The other microscopy methods employed are the SEM and TEM which give insight into the shape and morphology of the nanowires.

3.1.1 Scanning Probe Methods

MFM is part of the scanning probe microscopy (SPM) family which raster scans a surface and maps the interaction between a tip and the sample of interest. Two main modes employed in SPM are to keep the magnitude of the interaction constant by varying the tip-sample distance (constant force/current mode), or the spatial variation of the interaction is mapped by keeping a constant tip sample distance (constant height mode).

The constant ’interaction’ mode requires fast piezo actuators to change the tip-sample distance. The feedback system circuits involved always introduce a slight falsification of the ’topography’, an effect which can be minimized by adapting the feedback parameters according to the surface properties. A simple rule of thumb is: the rougher the surface, the faster and stronger the feedback has to react. This introduces noise and overshoot effects at large features. On the other hand if the feedback is too ’soft’, the ’topography’ is not represented accurately. The following is a quick overview over the most important variants of SPM, going into technical details only where relevant to the work discussed in this thesis.

The first SPM exploited the tunneling current between a sharp metallic tip and a conducting surface, this Scanning Tunneling Microscope (STM) was introduced in 1981 by Binning and Rohrer [32]. The main drawback was the limitation to conducting surfaces as well as stringent environmental preconditions, Ultra High Vacuum (UHV) and vibrational damping.

Scanning Force Microscopy (SFM) is a variant which maps the interaction force between a tip at the end of a cantilever and the surface of interest. The oldest (1986 by Binnig et al. [33]) and most prominent example is Atomic Force Microscopy (AFM), utilizing the short range interaction between the ’tip atoms’ and surface atoms. There are two atomic forces involved, best illustrated by the force distance curve presented in Figure 3.1.

At relatively large distances attractive van der Waals forces dominate. At closer range, repulsive Coulomb forces begin to dominate. Various AFM modes work at different stages of the curve. In contact mode AFM the tip snaps into contact with the surface. The static deflection of the cantilever is used as feedback parameter. Intermittent contact mode (tapping mode) uses a cantilever driven to oscillate at its resonance frequency, the attractive force dampens the oscillation which is used as a feedback parameter. This mode works to the right of the attractive peak portrayed in Figure 3.1. Non-contact AFM also uses a driven cantilever, but in this mode either the phase shift between the driving and the cantilever oscillation or the shift of the resonance frequency is measured. If one goes further away from the sample, long range forces dominate. Electrostatic

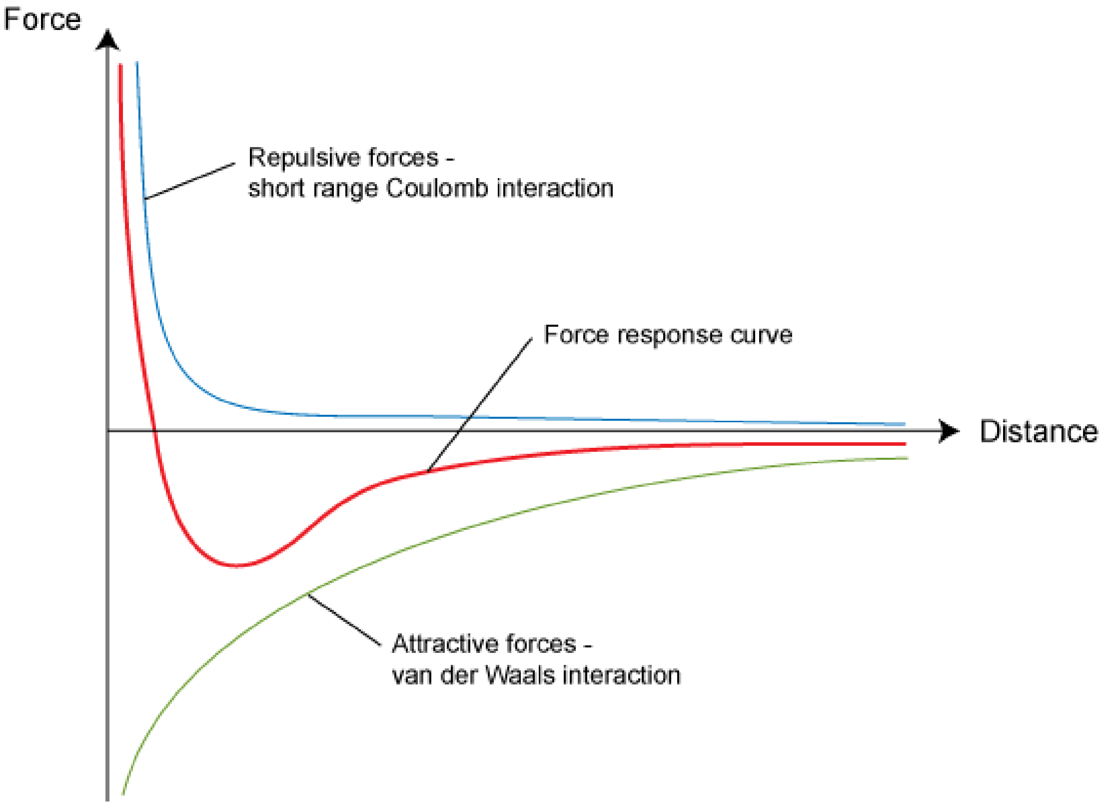

Figure 3.1: Schematic representation of the force distance curve.
Source: www.doitpoms.ac.uk/tlplib/afm/tip/_surface/_interaction.php

forces are always present to a certain extent, and magnetic forces if both the sample and the tip are magnetic.

Two methods exploit the long distance electrostatic forces between a conducting tip and the sample, Kelvin probe force microscopy (KPFM) and electrostatic force microscopy (EFM). KPFM uses an AC voltage along with a variable DC voltage to drive the cantilever [34]. EFM on the other hand works like a classical non-contact technique, the electrostatic forces shifts the dynamic properties of the driven cantilever. The force depends on the potential difference and contact potential difference, given by the work function for conductors. The electrostatic force is always attractive and can thus be used for a safe approach in other non-contact SFM modes. This works by causing a feedback response while still being at a safe distance from the surface. Such a 'safety margin' is particularly useful for high resolution non-contact MFM measurements. Before the aspects of MFM will be discussed in greater detail, two microscopy techniques are briefly explained which were crucial for the the physical characterization and sample preparation.

3.1.2 Scanning Electron Microscope

A crucial tool for locating and characterizing the nanowires is the scanning electron microscope (SEM). A FEI NanoSEM was employed, offering an acceleration voltage of up to 15keV, allowing one to image conducting surfaces with a nanometer resolution. The normal image is formed by secondary electrons expelled from the surface and collected by the two lens detector (TLD). Primary electrons which are reflected are called back scattered electrons, their intensity is dependent on the atomic number of the element, therefore the back scatter electron detector (BSED) allows one to identify Iron nanowires enclosed within the nanotubes and roughly measure their dimensions. Further, it efficiently contrasts Iron from both carbon and silicon, but not from the gold of the patterned elements.

3.1.3 Transmission Electron Microscopy

A transmission electron microscope (TEM), FEI Tecnai F30 with up to 300keV, was employed (by Markus Löffler and Uhland Weissker) to learn something about the physical characteristics like phase of the filling as well as the crystal orientation of a single crystal nanowire. It requires a separate sample preparation technique so it is not possible to image the same wire in the TEM and MFM as is the case for the SEM. A suspension of FeCNT is dropped onto a ClBr crystal until a thin film forms. The supporting crystal is then dissolved in distilled water, leaving a thin film or 'buckey paper' floating on the surface, ready to be collected with a copper TEM grid. Unlike SEM, TEM works with highly energetic electrons that pass through the sample, scattering in the process. Next to the obvious application as imaging tool it can also be used to conduct electron energy loss spectroscopy (EELS). By performing a fast Fourier transform routine on a section of the image one can identify the crystal structure and thereby the phase of Iron present. Phase is maybe not the most correct description of Iron carbide because it is a composite but the author adopts this notation common in the literature. Further, TEM is able to identify the crystal orientation relative to the CNT which is of particular importance for the Iron carbide filled nanotubes.

3.2 Magnetic Force Microscopy

Magnetic Force Microscopy (MFM), initially conceived by Saenz et al. [35] as well as Martin et al. [36] in 1987, probes the stray field emanating from a sample. This is achieved with a magnetic tip at the apex of a cantilever. The magnetic tip interacts with the stray field of the sample, changing the dynamic properties of the cantilever driven to oscillate at or close to its resonance frequency. A repulsive force causes an increase of the resonance frequency while an attraction has a decreasing effect, mapped as white and black contrast respectively. In the following section the separate components will be discussed on an individual basis, culminating into a complete picture of the instrument and the way it maps magnetic samples. MFM only works in the non-contact mode, since magnetic forces are weaker than atomic ones, however they are detectable over a longer range.

Two common MFM methods exist, lift mode and true non-contact mode. In the lift mode each line is first scanned in tapping mode AFM to measure the topography. The so measured surface contour is then retraced at a certain lift hight (50-100nm) to get an MFM picture. This technique is particularly useful for rough samples or where a correlation between topography and magnetic signal is present. The main drawbacks arise during the tapping stage, the tip has to be rigid enough to survive the tapping mode, which limits the achievable resolution. Further the tip is very close to the surface, which makes it more likely to influence the sample's magnetization, falsifying the measurements. True non-contact MFM on the other hand scans in a constant plane over the surface, at a safe distance, thereby allowing for sharper tips and higher resolution. This technique only works on relatively flat samples, and topographic influences, visible as EFM contrast can only be excluded when performing the same scan at opposite tip magnetizations.

3.2.1 Principle of Magnetic Force Microscopy

MFM maps the spatial variation of the magnetic field gradient. It achieves this by measuring the influence of a force on the oscillating behavior of a cantilever, felt by a magnetic tip at its apex. The force is given by

$$\vec{F} = (\vec{m} \bullet \nabla)\vec{B} \tag{3.1}$$

where in this case $\vec{m}$ is the tip magnetic moment, and $\vec{B}$ the sample stray field. This force shifts the resonance frequency of the cantilever as described below. Since the cantilever oscillates in the z-direction the MFM is only sensitive to the z-component of the force. Therefore one has to chose the tip magnetization so as to correspond to that component of the samples stray field one intends to study. In most cases the tip is also magnetized in the z-direction and is therefore sensitive to gradients of the z-component of the stray field.

3.2.2 The Tip

The most important contribution towards sensitivity and resolution is provided by the MFM tip. In most cases, including large part of the measurements presented in this thesis, an AFM tip is coated with a hard magnetic material. This results in a hollow magnetic cone or pyramid, the stray field of which is correspondingly hard to calculate. An MFM measures the second derivative of the z-component of the sample's stray field. To simplify the interpretation of MFM images the point probe approximation was introduced [37]. This makes it easier to interpret MFM images, especially when considering that the tip moment is strictly speaking not constant, but depends on the sample stray field decay length which decides how much of the tip 'feels' the feild.

In this work both self coated (by Joachim Schumans) high moment probes (Figure 3.2(a)) and specially produced low moment high resolution probes (provided by Nanoscan or Team Nanotec) portrayed in Figure 3.2(b) were employed. A third type of tip used to scan, but not for data presented in this thesis, were

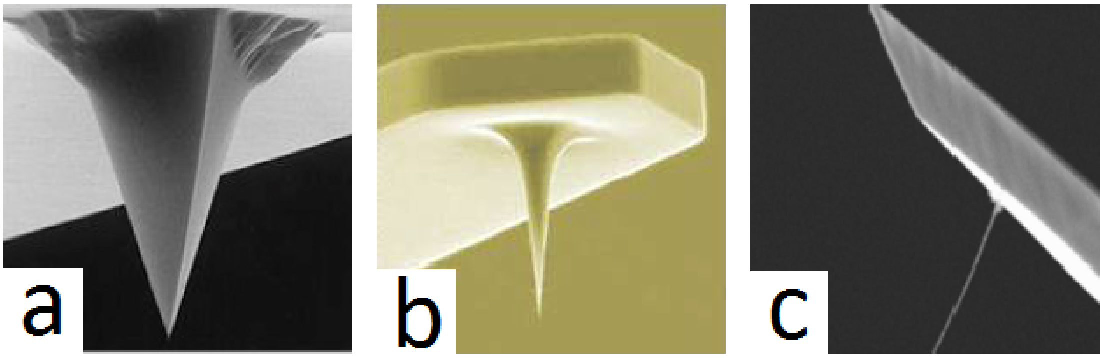

Figure 3.2: (a) A conventional pyramidal MFM tip (image from www.nanoworld.com). b) A high aspect ratio tip specifically designed for hr-MFM (image from www.team-nanotec.de). c) An Iron filled CNT attached to a cantilever (image courtesy of Franziska Wolny).

Iron filled carbon nanotube probes (Figure 3.2(c)) which have multiple advantages over coated probes as described in ([38]).

Tip properties like radius of curvature and durability are only partially relevant to MFM, since the magnetic resolution is always lower than the topographic one. This is due to the long range nature of magnetic stray fields, the tip does not only interact with the sample directly beneath it but also with the ambient stray field.

3.2.3 The Cantilever

The forces of interaction act on the tip, which is rigidly connected to a cantilever. These forces influence the oscillation properties of the driven cantilever. The cantilever is micro fabricated out of silicon or silicon nitride and its dimensions vary from 125 to 450 μm length, 28 to 40 μm width and 1 to 8 μm in thickness, depending on the desired properties. The material and the dimensions are decided for the specific type of application.

Depending on the type of cantilever and the conditions under which it is operated the sharpness of the resonance peak can vary greatly. A measure of this sharpness is the so called Q-factor which is the resonance frequency f_0 divided by the FWHM (full width at half maximum) of the energy vs. frequency graph.

A force gradient changes the effective spring constant

$$k = \frac{Ewt^3}{9L^4} = \frac{F}{\delta} \tag{3.2}$$

of the cantilever, thereby changing its resonance frequency.

$$\omega_0 = \sqrt{\frac{k}{m}} \tag{3.3}$$

Where E is the Young's modulus, w, t, L and m the width, thickness, length and mass of the cantilever respectively. The change in resonance frequency depends on the force gradient $\delta f \approx \frac{f_0 \delta F_z}{2k\delta z}$. An attractive force will cause a negative frequency shift and a repulsive one a positive shift. Since the amplitude is at a maximum at f_0 the precision of a feedback mechanism can be improved by measuring the phase shift, which is at an inflection point.

3.2.4 The Feedback Loop

The shift in the resonance frequency is detected by a complex feedback system. The phase shift between the driving and the measured oscillation is detected by a superLED and a photo detector. Depending on which type of MFM is employed the feedback is used to regulate two different parameters. In lift mode MFM the phase of the cantilever is measured, keeping other contributions nominally constant by following a prerecorded path above the surface. Constant height mode scans the tip in a plane above the surface, the driving frequency is adapted so as to keep the amplitude and the phase shift constant, the frequency shift being the measured signal.

Combining the basic principals discussed above one can start an MFM scan. Two different models where used for the measurements, utilizing two different approaches to measure the non-contact MFM signal.

3.2.5 Lift-mode MFM

The simpler of two methods mentioned above is the so called lift-mode. The tip is at first scanned in tapping mode above the surface, followed by a second scan of the same line but at a certain lift height above the prerecorded surface, a procedure necessary to account for non-magnetic interactions between tip and sample. The tapping procedure limits the array of applicable tips to those designed for this operation mode, requiring a certain stiffness of the cantilever and tip hardness, see Figure 3.2. This technique has the advantage that one gets topographic and magnetic information at the same time. Further the setup is much simpler, as it works under ambient conditions. The sensitivity to topography also allows one to image samples with a roughness of several micrometers such as cells. The MFM employed for the lift mode studies was a Veeco DI 3100, with a scan range of 90*90 μm.

To load a sample one has to open the damping hood and place the sample on the measuring table. This can then be moved under the retracted tip. To approach the tip one focuses on first the tip and then the surface, inputing the focal plane of the camera into the software. The first coarse approach is then initiated automatically, followed by a gradual approach until the surface is reached.

3.2.6 High Resolution MFM

Most of the data presented in this thesis were measured with a high resolution MFM (hr-MFM) provided by the company Nanoscan. It is a high vacuum system, specialized on non-contact MFM. In this mode the tip always maintains a safe distance to the sample, the signal is the value of by how many Hertz the driving frequency was shifted to maintain a maximum oscillation amplitude and a constant phase shift. Avoiding contact with the surface allows for the application of high aspect ratio tips (Figure 3.2(b)) which are too brittle for tapping mode, increasing the achievable resolution. The vacuum ensures a sharp resonance peak as well as thermal stability which, when combined with the rigid body of the microscope and an active damping table, ensures a high scanning stability and high signal to noise ratio. This also allows one to use a low moment probe, since less interaction is required which has the advantage of reducing the undesired influence of the tip on the sample which can cause premature or repeated switching. A drawback is that the scan range of 40 by 40 μm required careful positioning beforehand, which is quite challenging considering this is done with the aid of cameras from outside the vacuum chamber.

3.2.7 Magnetic Field Options

To study the switching behavior of magnetic nanoparticles one has to be able to apply magnetic fields. This is achieved by two additions to the system: the Perpendicular field option (PFO) is a bar magnet on a retractable shaft, approached to the sample from below. The maximum field applicable depends on the set up used for measurement (see below) but was 600 mT for most experiments. The in-plane field option (IFO) consists of four bar magnets arranged in the scanning plane, so as to cause a field along the x direction the magnitude of which can be controlled by the y-position. The maximum achievable in-plane field was 240 mT. The y-position is changed by sliding the whole construction along rails, powered by a (zitter) piezo. No errors are stated for the applied field since was not possible to determine them precisely. The installation and optimization of the IFO will be discussed in more detail since it was performed by the author in collaboration with the supplying company.

3.2.8 In-Plane Field Option Optimization and Calibration

The IFO was developed by Nanoscan and built at the (Institute for Solid State Research) IFW Dresden, it was a prototype which still had to be calibrated and as it turned out optimized. The calibration procedure was carried out by placing a hall probe at the position of the tip. The x-component of the stray field was then measured for the entire y range of the IFO, the results of this calibration procedure are presented in Figure 3.3.

Already during the calibration procedure it became obvious that the sledge system was not really running smoothly, it got stuck frequently and had to be freed manually. This would mean venting the chamber, a time consuming

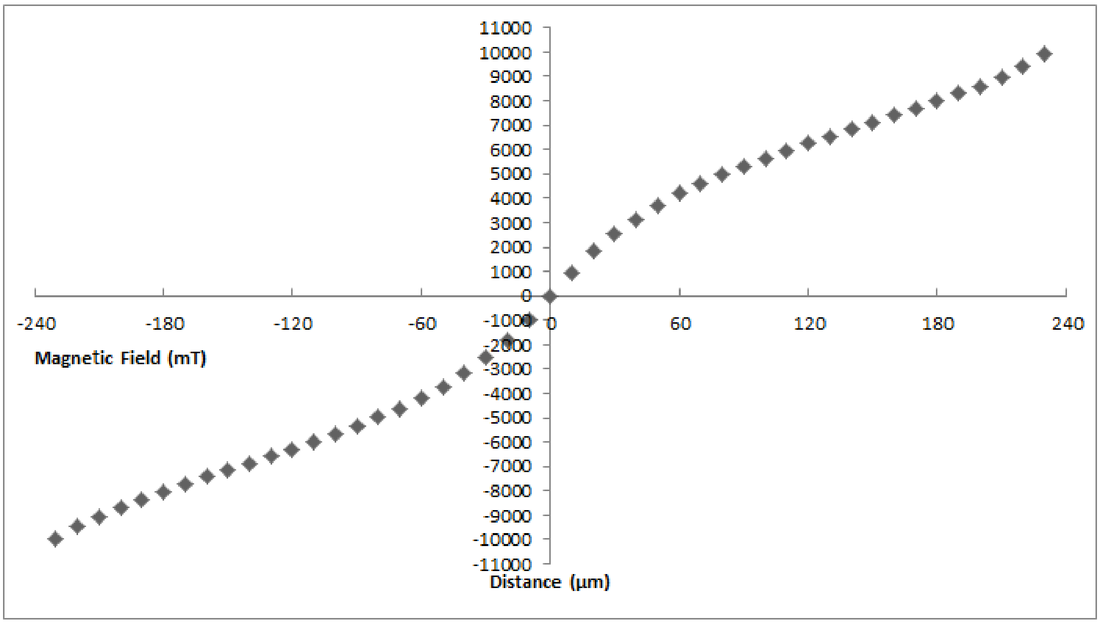

Figure 3.3: Raw data of the calibration procedure.

procedure. To reduce the possibility of the IFO getting stuck one of the clamps and piezos was removed, so as to avoid over restricting the movement. Unfortunately this did not deliver the desired improvement and brought new problems. Since the sledge was less restricted it was possible for the holder and thus the sample to move by a couple of millimeters, which required one to check manually if the sledge was aligned properly at the beginning of each measurement.

Before the details of the MFM measurements are discussed, the production routes and preparation steps towards measurable nanowires will be explained.

3.3 Nanowire Production

The principles and experimental details of the employed methods are important to understand the resulting magnetic properties. The two types of nanowires explored in this thesis are different in most aspects. The routes toward obtaining the final wire are briefly explained below for completeness. For a more detailed description the reader is referred to publications of the colleagues responsible where relevant.

3.3.1 Chemical Vapor Deposition

The process of chemical vapor deposition (CVD) is the most widespread route to producing CNTs and is currently employed to produce large quantities, mainly for composites. A connection between the experimental details to the resulting magnetic properties will be drawn in the results and discussion section. The main apparatus involved in the production of CNT is the oven, which creates a hot zone where the reaction takes place. Argon is most often used as an inert carrier gas, transporting the carbon source (hydocarbon gas or vaporized liquid) and hydrogen into the hot zone where it encounters the substrate. The substrate is covered in a catalyst which breaks down the carbon source, absorbs the carbon molecules and once saturated expels them in crystalline form as carbon nanotubes.

Iron nanowires can form withing the CNT without the addition of Iron into the source gas, when the catalyst particle seeding the growth gets dragged along with the growing tube. Such wires are very short and only found at the base of the CNT, which also accounts for their irregular shape. To obtain long, straight nanowires over the entire length of the nanotube, additional Iron has to be introduced into the hot zone, where the growth takes place. The most common source of Iron is ferrocene, $Fe(C_5H_5)_2$, an organometallic complex. There are various means of introducing ferrocene, either in gaseous form or as an aerosol. Not only the gas mixture, additional injection of ferrocene and the oven geometry and temperature can be varied, the catalytic precursor also comes in various forms. The sample can either be grown on an oxidized silicon wafer covered in a catalyst layer, or in the so called fixed bed method where the catalyst is part of a loose powder. The former produces a forest, with varying degrees of alignment, whereas the later results in a totally disordered 'wool'.

The α-**Fe** filled CNTs come from various batches, grown under different conditions. The main factors for successful Fe-CNT growth are control over the atmosphere inside the chamber, gas composition and pressure as well as temperatures on the one hand, and the catalyst and/or Iron source on the other hand. Multiple different furnace designs and methods of ferrocene injection were utilized to obtain α-Fe filled CNT, the precise description of which is beyond the scope of this thesis. The reader is referred to the publications of the colleagues who produced the corresponding CNT, Müller et al. [39], Hampel et al. [40], and Costa et al. [41].

The **Fe_3C** filled CNTs were the result of a slightly different experimental procedure. The growth was performed by Weissker et al. [42], following a recipe by Wang et al. [43]. Interestingly the two experiments yielded different results, while Wang obtained α-Fe filled tubes, Weissker found his tubes to be filled with Fe_3C. This discrepancy can probably be attributed to the different furnaces employed, especially the method of injecting the ferrocene dissolved in dichlorbenzene is significant.

Fe_3C filled nanotubes are grown at 830°C at atmospheric pressure. The precursor solution (60mg ferrocene $Fe(C_5H_5)_2$ dissolved in 1 ml of 1,2-dichlorbenzene $C_6H_4Cl_2$) was nebulized with an Argon flow of 300 SCCM (Standard Cubic Centimeters per Minute) and transported to the hot zone with aid of 300 SCCM of Hydrogen and 400 SCCM of additional Argon. In the hot zone the gas mixture encountered the silicon/silicon oxide substrate covered in a catalytic layer consisting of 10nm of of aluminum and 0.5 nm of Iron. After the reaction time of 10 minutes the oven was allowed to cool.

3.3.2 Tailored Nanowires

To control the magnetic properties of nanowires one has to be able to tailor their dimensions. The method of choice for producing large and regular arrays of nanowires is metal deposition onto a polymer layer which was partially removed by e-beam lithography in a scanning electron microscope (SEM).

The **Electron beam lithography** (EBL) was conducted with the aid of Kamil Lipert. An oxidized silicon substrate (1*1cm) was thoroughly cleaned and placed into the spin coating apparatus. The sample was rapidly rotated and a drop of poly(methyl 2-methylpropenoate) (PMMA) with a molecular weight of 950K and 9% chlorobenzene content was applied. After a short drying interval a second layer of a PMMA with shorter polymer chains was applied (molecular weight 50K and 1% chlorobenzene). The bottom layer is more sensitive to damage by electrons, meaning it will react stronger during the development process, creating an overhang upon development. This assures a clean lift-off as explained below.

The layout of the nanowires was planned with the Edraw^{TM} software. It is important to carefully plan the process, especially a continuous movement of the electron beam between individual elements of the patterns. If the beam has to jump during the process, it is very likely that small areas are not exposed or doubly exposed, both cases lead to grave errors in the final patterns. The layout of each element can be duplicated at will, creating very large arrays. The beam size can be adapted which makes it easier to create rough large structures which are used for orientation. The meta pattern, consisting of a map of rough structures and various patterns of the actual wires under study, can also be duplicated.

The completed pattern is then transferred onto the control computer of the EBL set up, where it loaded into the Elitho^{TM} software which directly controls the beam of the SEM. The details of the exposure process are beyond the scope of this thesis, but a simple picture is that the electrons break the polymer chains, allowing them to be dissolved in the next step of the process.

The exposed sample is then placed into a Methyl Isobutyl Ketone (MIBK) and Isopromanol mixture (1:3 volume ratio) for 3 minutes. At this stage the exposed sections are removed at a much higher rate than the unexposed ones. Exact timing is essential, so as to not overdevelop the structure and thereby compromising the quality of the final product. The development is stopped by placing the sample into pure Isopropanol and then allowed it to dry.

The **Metal deposition** was performed by Joachim Schuman. The entire sample is covered with a 50nm layer of permalloy. The covered substrate is placed in an acetone bath, which dissolves the remaining polymer sections, causing the metal on top to lift-off. Only the metal which landed on the exposed section, thus directly on the substrate, remains.

3.4 Sample Preparation and Analysis

Depending on the precise CVD method employed the as grown sample is a forest or bundle of nanotubes which are not suited for MFM unless further processed. To find suitable wires and study the crystal structure SEM and TEM respectively were employed.

3.4.1 Dispersion

To obtain separated nanotubes the as grown forest was placed in acetone and ultrasonicated. Exposing nanotubes to extensive ultrasonication can damage and shorten the CNTs. Part of the dispersion procedure was therefore carried out with a mechanical stirrer. The dispersion was then pipetted onto a specially prepared substrate, leaving separate CNTs after the acetone evaporates.

3.4.2 Substrate

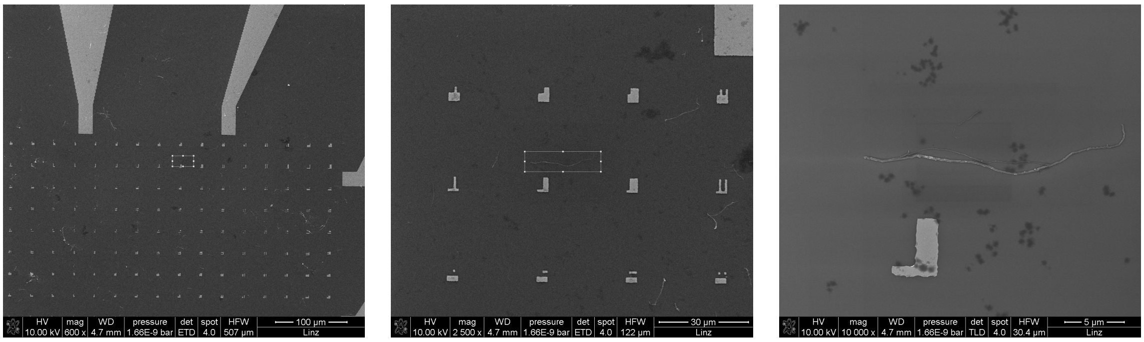

Figure 3.4: SEM images of: (left) large fingers, (center) array of elements, (right) a single element.

The substrate (Figure 3.4)used for the study of individual CNT has to fulfill certain requirements. It has to feature elements which are large enough to be recognized with the CCD cameras of the MFM, of the order of 100 μm ('fingers'). Further unique elements of the order of 4μm are required which are used to map the location in the SEM and can then be identified in an AFM/EFM scan. This is achieved by a photo lithographic process (perfomed in house by Mönch et al.)

An oxidized silicon substrate is covered in a photo resist. A mask covers the desired area of the elements. UV-light is used to destroy the polymer structure of the photoresist, followed by a wet chemical etching which removes the exposed section. The whole wafer is then covered by a thin layer of gold. The procedure is finalized with a lift off procedure, where the photo resist is dissolved, taking the undesired gold sections with it. What remains are the elements.

3.5 Measurements

Both MFMs employed offer a large area for samples, due to one of their main applications being the study of hard discs. The Veeco dimension has a remote controlled table onto which the sample plate is placed, and then navigated under the tip. For the hr-MFM the sample is glued to a sample disk using silver glue, the whole disk is then mounted onto the motor table. The disk can be rotated and the tabled moved in one direction.

3.5.1 Embedded Forest

A well aligned forest can be covered in tetraethyl orthosilicate (TEOS) and then polished down to a flat surface [39]. This results in an array of Iron nanowires perpendicular to the surface, so only the signal from one end is measured by the MFM. This is however sufficient for switching studies when assuming single domain wires.

3.5.2 Individual Wires

For the complete picture of an Iron nanowire one needs to look at it along its entire length, so they have to lie flat on the substrate.

To get the nanotubes onto the substrate they were dissolved in acetone and dropped onto the substrate. The central section of the patterned substrate with the applied nanotubes was then investigated with the SEM BSED (Figure 3.4(a)), looking for nanotubes containing high quality wires. The location of the wires relative to the patterns and 'fingers' was mapped and measured using the SEM software. Due the inability to contrast Iron from gold only wires found in between the markers were imaged. The information gained from the SEM studies then allows one to find the same individual wires for the MFM scan. The fingers can be recognized in the camera of the MFM, allowing one to position the tip in the proximity of the wire. A large area MFM scan with strong bias applied reveals the small marker structures. If the wire is within the scan area, one can simply zoom in on it. If it is located outside, one can use a map of the small patterns to move the scan area of $40\mu * 40\mu$ to the correct location. Once the wire is identified, the bias is reduced while simultaneously lowering the tip. The electrostatic contrast of the CNT disappears revealing the magnetic signal of the enclosed wire.

3.6 Applying Magnetic Fields

MFM images allow one to assign a direction to the magnetization direction of a single domain particle, information which permits one to draw conclusions about the dominant anisotropy contribution and in certain cases the crystal orientation. A more complete picture can be drawn when applying external magnetic fields at different angles. The switching field can be used to calculate the strength of the magneto crystalline anisotropy in single domain particles, dipolar interactions in arrays or other effects in spin ice structures. The angle dependence of the switching field can reveal the mechanism of magnetization reversal.

When the **PFO** is employed a special sample disk has to be used, to allow the magnet to approach from below. This disk consists of an extension in the form of a plate with a hole at the end. Over this hole a thin strip of silicon substrate is placed as a bridge, on top of which the sample is mounted. When applying the field it is important to constantly readjust the center frequency in the feedback loop settings, since the applied field causes a constant force on the tip. The reason for manually adapting the center frequency is mainly to maintain the function of the automatic abort mechanism, which retracts the tip when more then 20Hz (set by user) shift is detected.

For applying the **IFO**, the piezo rails have to be attached to the microscope head. Then the platform is attached to the rails and retracted to the maximum possible distance. Only now the tip holder is placed into microscope head. After moving the piezo platform to the center position, the plate containing the four magnets is set into the piezo platform, taking care to keep it centered over the tip so as not so influence its magnetization. Once the magnets are in place it is not possible to change the magnetization of the tip. Since the tip is located in the center between the magnets, also in the z-direction, the sample has to placed on a tower. Further the sample has to be smaller than usual, a maximum of 4*4 mm.

The theory and aparati presented in this and the previous chapter have prepared the way to investigate the experimental results presented and discussed in the next two chapters as well as understand their significance.

Results and Discussion I
- Iron Filled Carbon Nanotubes

An overview of the experimental results on iron filled CNTs and a discussion of their significance. The findings will be grouped into two sections, alpha iron filled CNTs and iron carbide filled CNTs, each starting with structural investigations followed by MFM studies of their remanent magnetization and switching behavior. Some of the hr-MFM images presented in this chapter were processed by cutting off peaks and troughs of the signal (represented by red and blue contrast respectively) in order to make weaker contrast visible. Finally the discussion for each part, making use of theoretical concepts discussed in the theory chapter, will be wrapped up by a comparison of the two types of wires.

4.1 Alpha Iron Filled CNT

Carbon nanotubes are the ideal material for filling, they act as stiff cage and protect the filling and the environment from each other. In the case of α-Fe wires encapsulated by CNT, a protection against oxidation is warranted, maintaining the magnetic properties.

4.1.1 Physical Characterization

Alpha iron filled CNTs were grown by various collaborators via CVD with ferrocene as a precursor. A substrate covered with a metallic catalyst layer is placed into a CVD oven with controlled temperature and atmosphere. The CVD process, the mechanism of CNT growth and aspects concerning the filling are briefly discussed in the methodology chapters for completeness.

Figure 4.1(a) shows an as-grown forest of partially filled CNT. Most of the wires found within the CNT have a length between 100nm up to several microns,

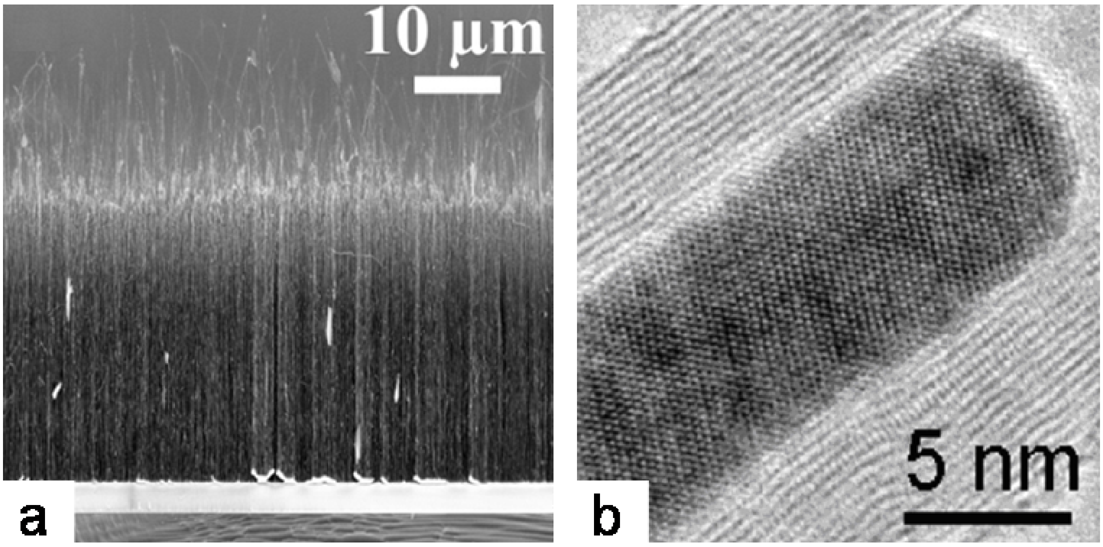

Figure 4.1: (a) SEM images (courtesy of Uhland Weißker) of an as-grown Fe-CNT forest [44]. (b) TEM images (courtesy of Markus Löffler) of an α-Fe nanowire showing the bcc crystal structure [44].

with a wide quality range. All CNTs used here were grown as such a dense forest and then processed according to different sample requirements. A stable array of vertical Fe-CNT was obtained by depositing SiO_2 onto an as grown forest followed by mechanical polishing to a flat surface [39]. Samples with individual Fe-CNT can be prepared by ultrasonicating an as grown forest in acetone and dropping the resulting solution onto a substrate. By dropping a solution of Fe-CNT onto a bromide crystal which is then dissolved in distilled water, a thin film is obtained which can be placed in the TEM. Such TEM investigations give a better view of the wires inside the CNT as shown in Figure 4.1(b). The phase of the filling can be identified from a Fourier analysis of the according image section in Figure 4.1(b), as being bcc ($a = 2.867$Å), belonging to α-Fe which is ferromagnetic and stable at room temperature. The filling depicted in Figure 4.1(b) is single crystal and of near cylindrical shape. Encapsulating the single α-Fe crystal one can clearly see roughly 15 shells of the MWNT. There seems to be a clear boundary between the wire and the innermost nanotube wall, as the diameter remains roughly constant in the filled and empty section. This is not always the case for filled nanotubes as shown for example by Löffler et al. [45].

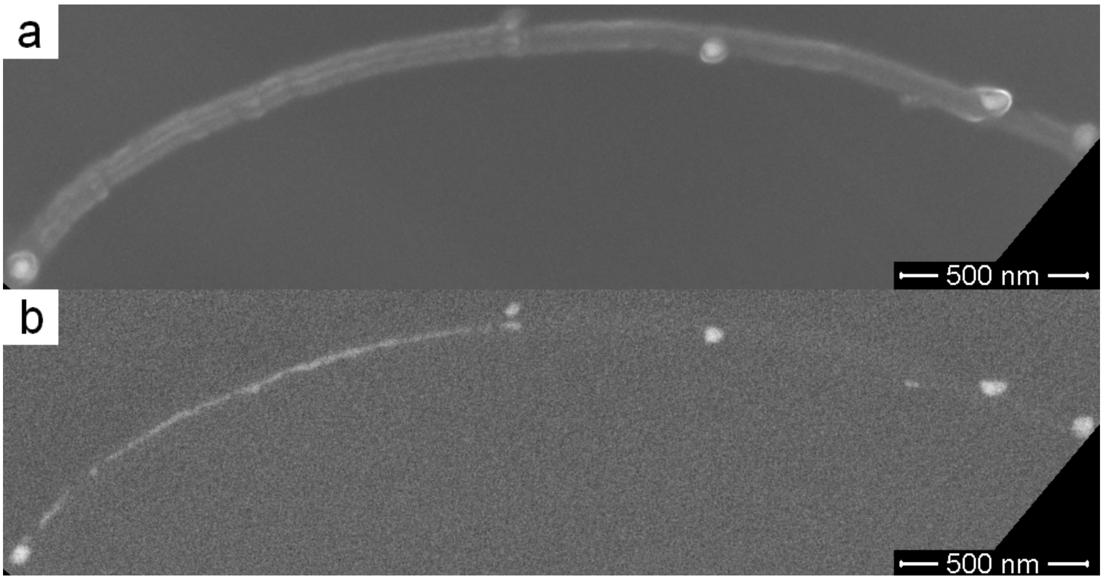

Figure 4.2: (a) SEM image recorded with the TLD, showing a Carbon nanotube with a slight signal from the filling. (b) SEM-BSED image at the same location, highlighting the filling.

The SEM analysis of wires deposited on a substrate highlights the large range of wire quality. Figure 4.2 shows the same section of filled CNT using the TLD (a) and BSED (b). While the first clearly shows the Carbon nanotube, the later is mainly sensitive to the filling. One can clearly see the long but irregular wire on the left as well as spherical particles on the outside on the right hand side. The case is different for the CNT viewed in Figure 4.3, where the tube itself (a) is shorter and very irregular, but especially the filling (b) is very fragmented and inhomogeneous.

4.1.2 Magnetic Characterization

Under the MFM such a filled CNT reveals dipolar contrast for each wire, as seen in Figure 4.4. Each wire visible in the SEM-BSED image (a) is seen as a dipolar contrast in the MFM image (b).

Similar results were found for all filled sections of CNT. Figure 4.5 shows the raw MFM data for a series of wires inside a CNT, the one on the left being more than 1.4 μm long, (a) and (b) differ solely by the orientation of the tip

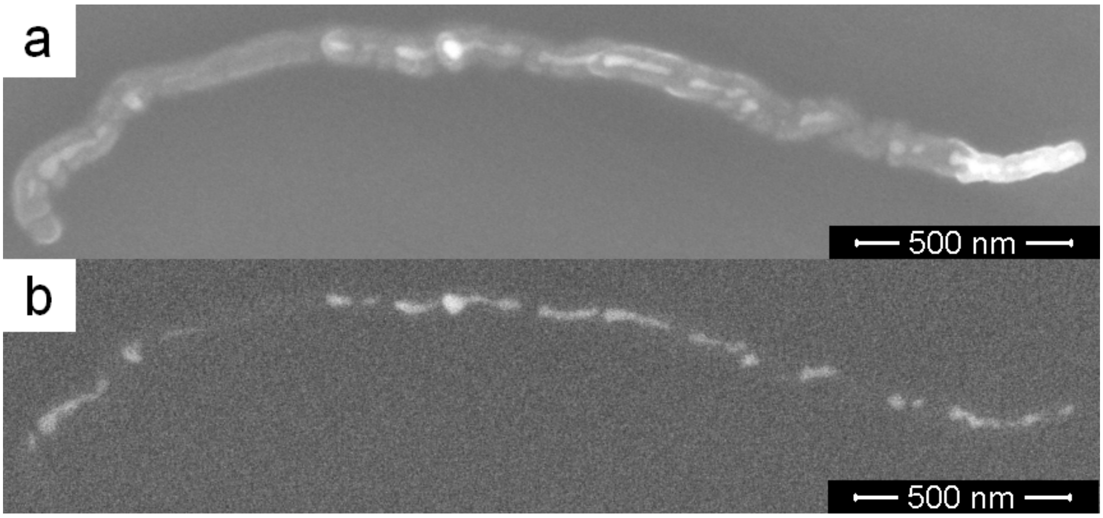

Figure 4.3: (a) SEM image recorded with the TLD, showing a Carbon nanotube with a slight signal from the filling. (b) SEM-BSED image at the same location, highlighting the filling.

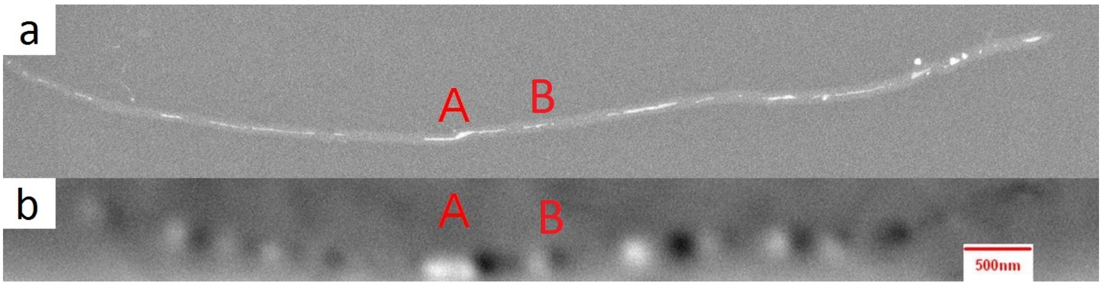

Figure 4.4: (a) SEM-BSED and (b) MFM image of α-Fe wires within a CNT.

magnetization. In some cases a very irregular shape can cause extended contrast as for example wire A in Figure 4.4. This is due to the limited magnetic resolution of the MFM caused by multiple surface stray field sources overlapping. Slight diameter variations also lead to weak signals along a wire, as seen in Figure 4.5. Nevertheless the majority of wires are of adequate quality and sufficient length to yield a dipolar contrast.

The reason that α-Fe filled tubes exhibit poles over the ends of the wires is that they are magnetized parallel to the long wires axis. This means that the stray field of the wire appears like an extended dipole or in the simple picture a bar magnet. The MFM images of α-Fe nanowires are a map of the derivative of

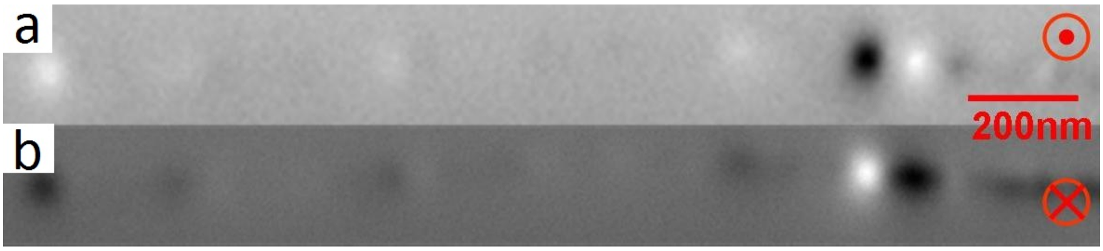

Figure 4.5: hr-MFM image of a long α-Fe wire within a CNT. Tip magnetization down (a) and up (b).

the z-component of the stray field, thus one can assign 'north' and 'south' poles to the wire by considering the according contrast. As discussed in the theory chapter, α-Fe has a very low MCA (0.048MJm^{-3}) due to its cubic structure and the quenching of the orbital moment typical for 3d metals, leaving the shape anisotropy (0.96MJm^{-3}) as clearly dominating factor. The high saturation magnetization of α-Fe is responsible for the strong shape anisotropy, which leads to a very high theoretical switching field, given by ($H_A = 2K_1 / M_s$), of 1.1 T. Up to 0.891 T switching field for good quality wires were found for samples from the same batch using micro-Hall microscopy at low temperatures [46].

The switching behavior of such a uniformly magnetized nanowire is of great interest for modern applications. The filled CNT displayed in Figure 4.4 was exposed to a magnetic field along the wires' axes with the aid of the in-plane field option (IFO). The switching of the wire labeled B in Figure 4.4 is observed at a field between 150 and 200 mT as presented in Figure 4.6. The remaining contrast remains qualitatively constant showing that the magnetizations of the the other wires as well as that of the tip remains unaltered.

For this individual wire set-up, the hr-MFM can only measure the rough switching field of a nanowire, since the in-plane magnetic field can only be altered in course steps. The instability of IFO meant that only the switching of one wire (both directions) could be observed in this fashion. To study the switching behavior of a large number of α-Fe nanowires a magnetic field is applied parallel to an embedded forest acting as an inhomogeneous and low density (2-3 wires/μm^2) array of vertically aligned α-Fe nanowires with an estimated diameter variation

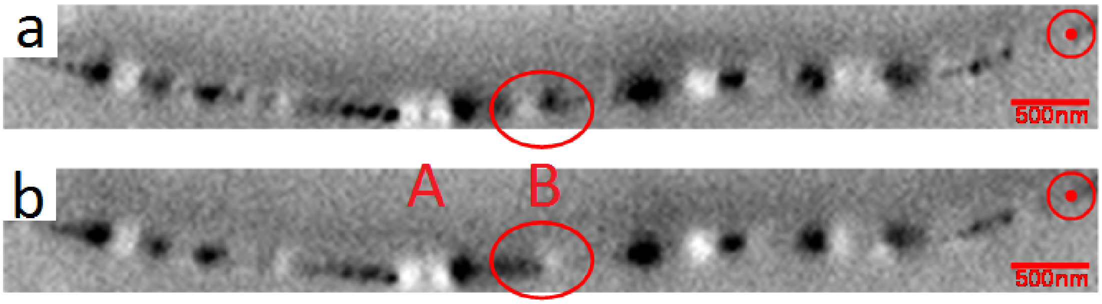

Figure 4.6: hr-MFM image of the filled CNT after applying (a) 150 mT and (b) 200 mT antiparallel to the wire magnetization, wire B is highlighted by red circles and the tip magnetization indicated in the top right corner

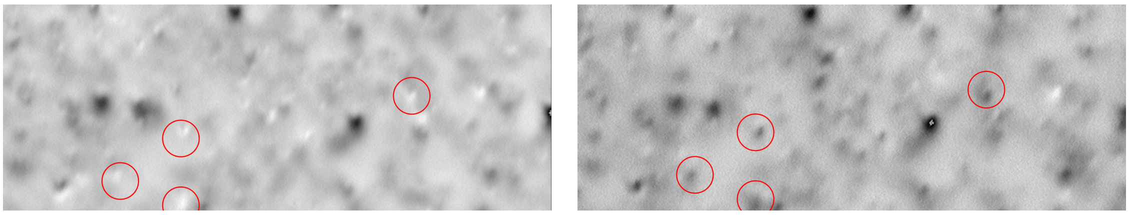

Figure 4.7: hr-MFM scan (8*3 μm) of the 58 nanowires after applying (left) 200 mT and (right) 325 mT [44].

of 12-26 nm [39].

A MFM image (two examples are presented in Figure 4.7) is taken for each field value, from which the magnetization direction of the 58 wires is determined. This was achieved by creating a template which was then placed over the MFM image followed by a manual count of how many of the corresponding signals had changed sign. The sample was initially saturated at -600 mT, and then exposed to increasing positive fields. The tip switches first, meaning that positive (white) contrast in Figure 4.7 represents an unswitched nanowire (antiparallel to tip), while negative (black) contrast can either be a switched (parallel to tip) nanowire or a structural artifact (acting through an EMF signal). As a consequence it first had to be determined which contrast is due to a wire, then a template was fashioned and masked over all pictures to determined how many wires had switched at each field value. The resulting count of switched wires from the according images can then be compiled into a hysteresis curve (Figure 4.8) by plotting it against the value of the applied magnetic field.

Comparing these results to measurements taken on α-Fe nanowires in porous aluminum [47] gives a similar result. Despite the similar shape, the switching field distributions are of different origin. The templated wires (uniformly and densely arranged with a very narrow diameter distribution) have a switching field variation as a result of dipolar interaction. The embedded Fe-CNT on the other hand are less densely packed and not spaced out uniformly, the switching field distribution is a result of the diameter and length variation of the wires. Shorter wires have a lower shape anisotropy which results in reduced switching fields. The diameter comes into play if a curling mechanism is involved which is discussed below.

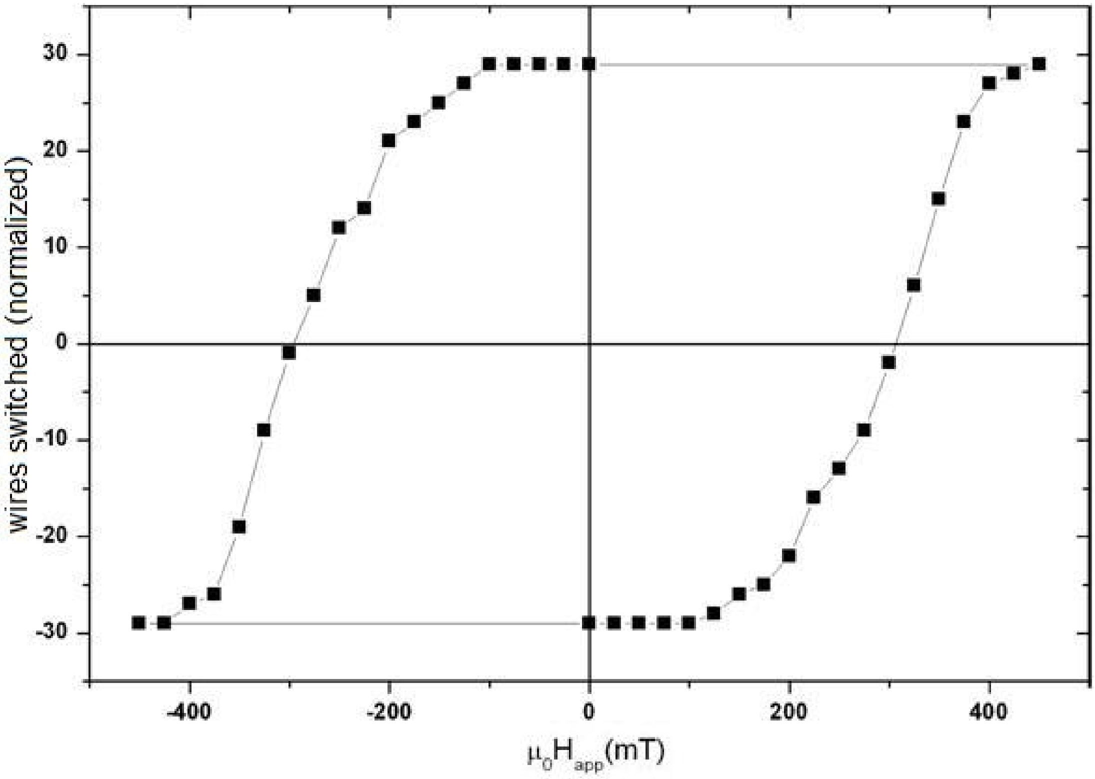

Figure 4.8: Data showing the successive switching of 58 individual α-Fe wires. Each data point corresponds to a MFM scan as presented in Figure 4.7. Sample was initially saturated at -600 mT. The line connecting the data points is a guide to the eye [44].

The data presented in Figure 4.8 was compiled from scans taken after the applied field was removed. Scanning under an applied field gives a different result, some wires switch earlier as seen in Figure 4.9.

The black data points (squares) presented in Figure 4.9 are the positive sweep from Figure 4.8, counted from an MFM scan taken at 0 mT after having applied the according field. The red data points (dots) represent counts from MFM scans taken while the external field remained applied, superimposing the highly inhomogeneous tip field over the larger and homogeneous applied field against which the count is plotted. The tip has a much lower switching field than the

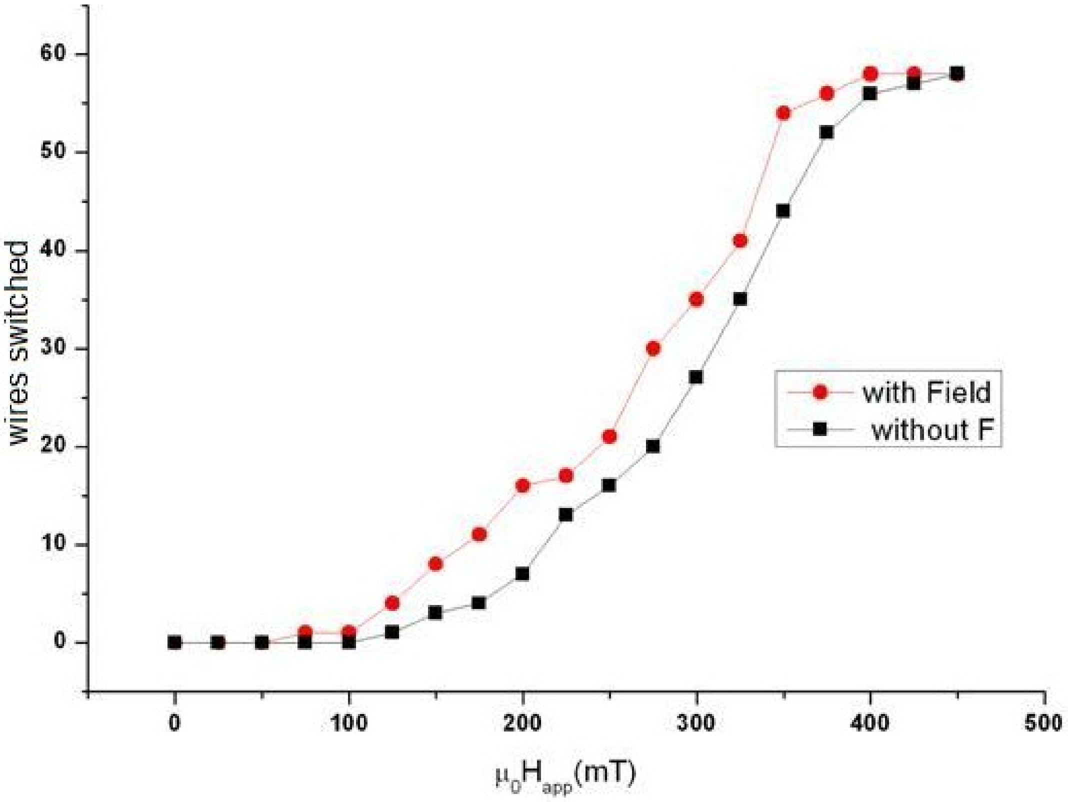

Figure 4.9: Data showing a comparison between scanning with the external field applied during scanning (red data points) and scanning after having removed the applied field before scanning (black data points = positive sweep from Figure 4.8). The line connecting the data points is a guide to the eye [44].

wires (roughly 20 mT), therefore the tip field will always be parallel the applied field in the range relevant to wire switching. For this study a conventional MFM tip with a relatively high moment was employed with resulting maximum tip field of approximately 35 mT [48], such a field approximately matches the shift in the measured switching fields. The tip field is comparatively weak and has a high gradient, so it can only have an effect in combination with the external magnetic field. The steep tip field gradient means that only the very top of the wires is exposed to the combined field. The fact that only a small part of the wire is exposed to a field sufficient for switching indicates a reversal of magnetization by localized nucleation [49]. Wernsdorfer et al. [50] reported such a process in deposited Nickel pillars. A nanowire within a CNT from the same type as used for the experiments presented in this thesis was studied by Lipert et al. [46]. They find that a small volume which underwent a curling magnetization reversal nucleated a domain wall which propagated through the remaining wire. Banerjee et al. [51] studied the reversal a similar α-Fe filled CNT with vibrating cantilever magnetometry at low temperature finding a thermally activated switching. All these methods measure individual nanowires which involve complicated sample preparation steps, as is also the case with the techniques used in this thesis. This means that it is very time consuming to get data for a large number of wires. Here the hr-MFM with the aid of the PFO proves effective, as demonstrated in the results on the embedded forest (Figure 4.8). This type of sample does not allow for a precise physical characterization of the individual wires and does therefore not exploit the full potential of this multi wire approach.

The data presented in Figure 4.9 can be explained when assuming that the tip field initiates a nucleation event by locally (top end) providing a field sufficient for switching. From the MFM data, no conclusions can be drawn about the reversal mechanism of the switching caused by the external field alone, but it is very likely that the same wire will switch by the same mechanism, in the later case the nucleation could be initiated at a structural inhomogeneity at a higher applied field.

4.2 Iron Carbide Nanowires

As before, the Fe_3C nanowires take form within the hollow of multiwalled CNT during the CVD growth process, conducted by Uhland Weissker [42]. With wire diameters in the range of 10nm they are thinner than nanowires studied by Silva et al. [52] at low temperature and by Belliard et al. [53] at room temperature with the MFM which also show transverse magnetization. Such thicker nanowires tend to show domain patterns. The Fe_3C nanowires on the other hand lie below the single domain limit, accounting for the continuous contrast presented below.

The presence of a sufficient amount of iron is warranted by the injection of a ferrocene aerosol into the hot zone of the oven, using dichlorbenzene as a solvent [42]. This process results in single crystal iron carbide nanowires of varying lengths, filling the hollow of sections of the CNT.

4.2.1 Physical Characterization

SEM and TEM were used to study the characteristics of the as grown material. TEM studies of the wires reveal that the b-axis tends to point along the hollow of the tube.

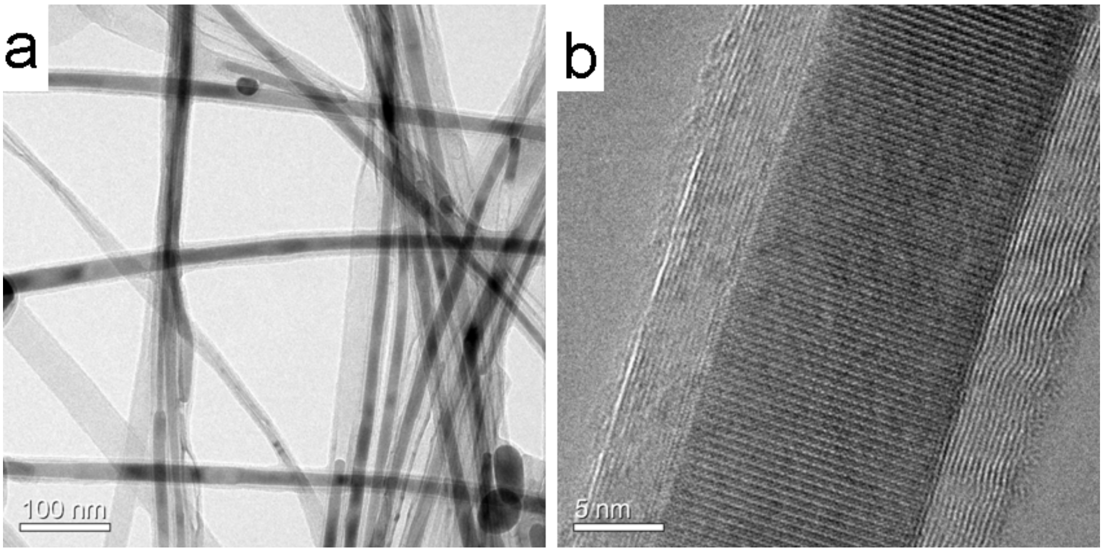

Figure 4.10: TEM pictures provided by Markus Löffler: (a) Overview over multiple filled CNT and (b) Crystal structure and Carbon shells [44]

The TEM pictures presented in Figure 4.10 clearly show the single crystal Fe_3C nanowires and the surrounding Carbon shells. Fourier analysis of the crystal structure shown in Figure 4.10(b) reveals that the b-axis is oriented along the hollow of the tube. This is confirmed for all iron carbide wires investigated with the TEM [42].

4.2.2 Formation

This trend can be explained by a phase transition during cooling, which leads to an expansion of the crystal. To specify, the author believes that Carbon saturated γ-Fe transforms into iron carbide upon cooling, with a resulting increase of volume. γ-Fe has a face centered cubic (fcc) crystal structure and does not order ferromagnetically.

Starting with the assumption that the Carbon saturated γ-Fe has the same fraction of Carbon as Fe_3C we can compare the volume of the two. The Carbon-content and temperature dependent lattice constant a_0 of γ-Fe [54] is given by

$$a_0 = [0.35519 + 8.1593 * 10^{-6} T K^{-1} + 1.7341 * 10^{-3} C] nm \qquad (4.1)$$

where T is the temperature and C the mass percentage of Carbon. Taking T as 1100K (CVD oven temperature), and C as 0.066 results in a lattice constant $a_0 = 0.365$nm. A fcc unit cell contains four atoms, giving the volume per atom as $1.22*10^{-2}$ nm^3. The temperature depended volume per atom for iron carbide (the Fe_3C unit cell contains four Fe and 12 C atoms) is given by

$$V(T) = \frac{a * b * c}{16} + 4.1 * 10^{-5} * T nm^3 K^{-1} \qquad (4.2)$$

where a, b and c are the lattice constants (0.4526nm, 0.5078nm and 0.6744nm) and T is the temperature (room temperature). This calculation yields a volume of $2.200*10^{-2}$ nm^3 per atom. This means that the volume of a Fe_3C nanowire compared to a Carbon saturated γ-Fe nanowire increases by a factor of 1.8. The rigid confinement of the CNT (maximum measured values for Young's modulus of 950GPa [55] and for tensile strength 150GPa [10]) and the elastic anisotropy (a = 596 GPa, b = 807 GPa and c = 649 GPa [25]) of the orthorhombic carbide crystal mean that the least energy is expended by forming the b-axis along the hollow of the tube. To elaborate: the system gains the most energy by expanding along the direction with the highest elastic modulus, and since expansion in all but one direction is hindered by the stiff cage provided by the CNT the b-axis will tend to form along the hollow of the MWNT as sketched in Figure 4.11.

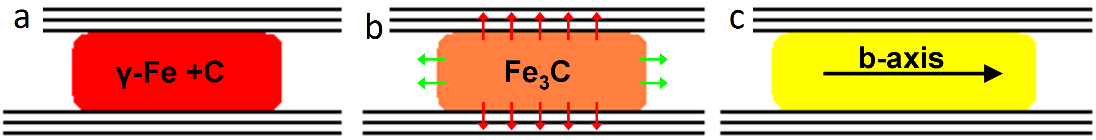

Figure 4.11: (a) Carbon saturated γ-Fe wire within CNT (b) Expansion as a result of Fe_3C formation upon cooling only possible along hollow of tube (c) b-axis has highest Young's modulus, forms along hollow.

4.2.3 Magnetic Characterization

The first MFM images of Fe_3C nanowires where taken with lift mode MFM (Veeco Dimension) and revealed an unusual contrast (not shown). Instead of having two poles at the ends, an extended pole was visible along the entire wire. This result was confirmed with the hr-MFM for a large number of wires, see Figure 4.12.

Figure 4.12 (a) shows two separate wires within the same CNT. From the MFM contrast (indicating a magnetization perpendicular to that of the tip) it can be assumed that the c-axis in both wires is close to parallel to the surface. This case is also observed in Figure 4.12 (d), where up to three wire segments are enclosed by the same CNT. The positive contrast at the intersection between the first and second wire segment could originate from a small additional Fe_3C enclosure, oriented perpendicular to the others. Figure 4.12 (c) shows two clearly separated wires, again both magnetized in the plane of the surface. The stronger contrast at left end of the left wire could indicate a diameter variation. The dark area over the left side of the right wire is an electrostatic artifact stemming from prolonged observation in the SEM.

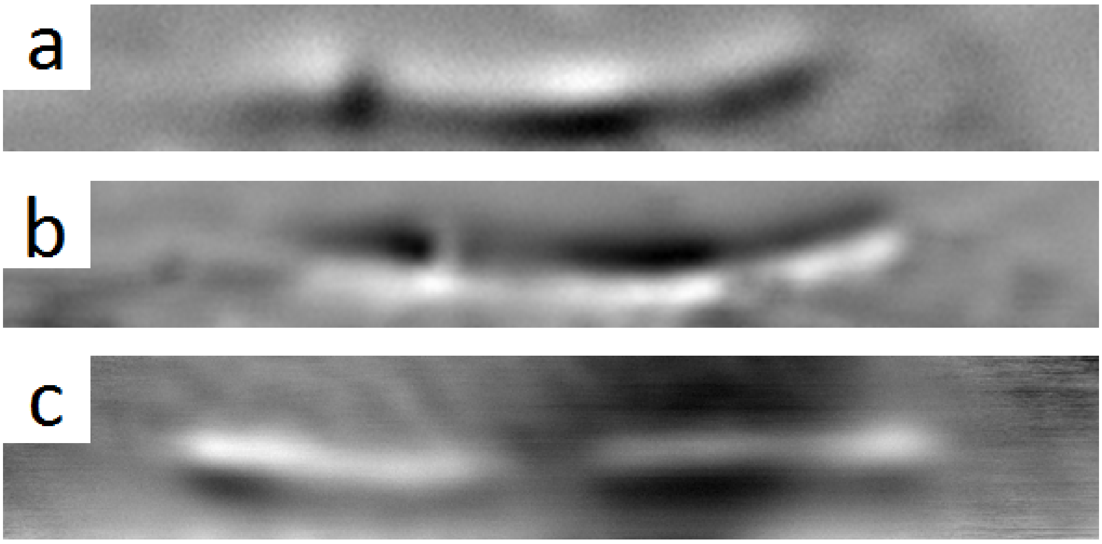

Figure 4.12: Three examples of wires magnetized close to parallel to the surface (a-c).

Figure 4.13 shows three wires enclosed in a bundle of CNT. The CNTs are clearly visible in the SEM-TLD image (a), while (b) highlights the wires by employing the BSED. The hr-MFM scan (c) reveals that the remanent magnetization is perpendicular to the long axis of the wire. In the case of wire **A** the magnetization is near to perpendicular to the tip magnetization while in the case of **B** and **C** it is near to parallel and antiparallel, as seen in the line section (yellow line defined in Figure 4.13(b)) presented in Figure 4.13(d).

An explanation for this magnetization arrangement can be found when comparing the shape anisotropy (SA) with the (MCA) and considering the preferential crystal alignment inside the nanotube. The MCA as measured by Blum et al. is $3.94{*}10^5 \mathrm{Jm}^3$ [26]. This value clearly dominates over the shape anisotropy ($3.06{*}10^5$ for a long wire) leading to a perpendicular magnetization. As the two anisotropy contributions are in competition the resulting effective anisotropy is small, resulting in a low coercivity.

This magnetic softness was already seen in the initial measurements (not shown) where the lift-mode scans caused a switching of the magnetization. To study this effect systematically both magnetic field options where employed. The effect of a perpendicular magnetic field is illustrated in Figure 4.14, were switching

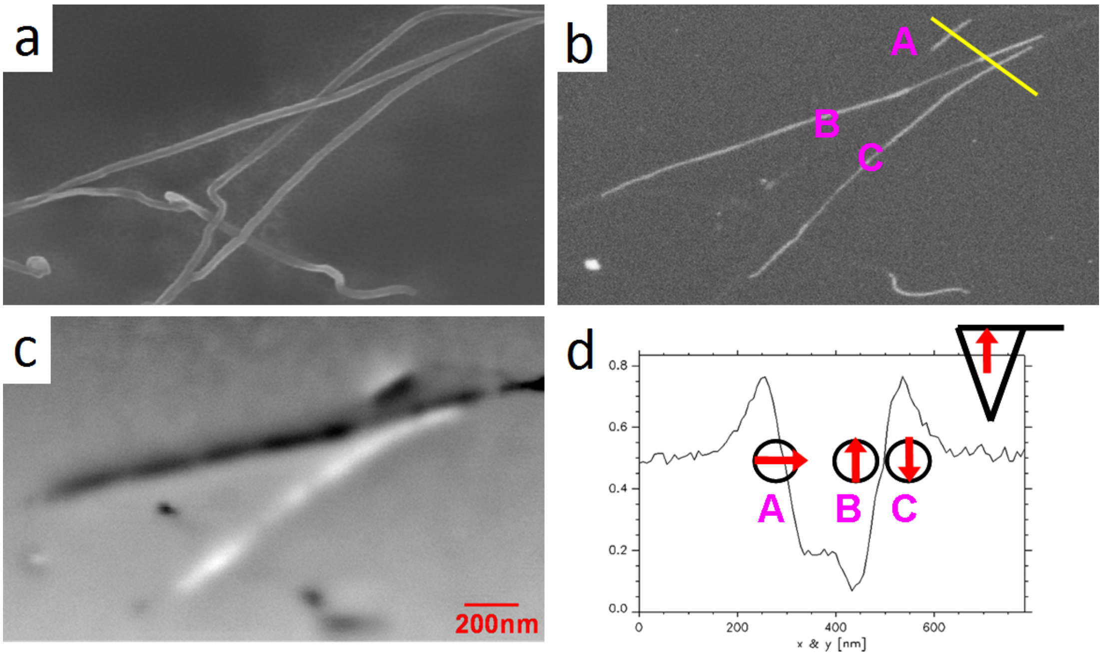

Figure 4.13: From [44](a)SEM-TLD image showing the bundle of CNTs. (b) SEM-BSED image showing Fe_3C filling, the three wires of interest are labeled A, B and C. The yellow line defines a cross section covering all three wires. (c) MFM image showing stray field derivative over the same area. (d) Line Section (defined in (b)) showing estimated magnetization direction relative to tip.

fields between 30 and 45 mT are observed.

Figure 4.14 (a) shows the MFM contrast and lines section (defined in Figure 4.13 (b)) after applying 9 mT. Comparing the contrast and line section to Figure 4.13 (c) and (d) respectively one notices the inversion of the signal, indicating reversal of the tip magnetization. Figure 4.14 (b) shows the case after applying the 30 mT, the field at which wire **B** switched. At 45 mT, shown in Figure 4.14 (d) wire **A** switched, indicating an out of plane magnetization component. For wire **A** the PFO result is for a field along the mid-hard axis, whereas for **B** (Figure 4.14 (b)) and **C** (not shown) they are along the easy axis.

To observe the corresponding easy and mid-hard switching fields as well as the hard axis switching fields for all three wires the IFO was employed. A fourth wire (**D**) contained by one of the same CNTs was included in these later measurements. Since the four wires are not oriented parallel a compromise had to be made,

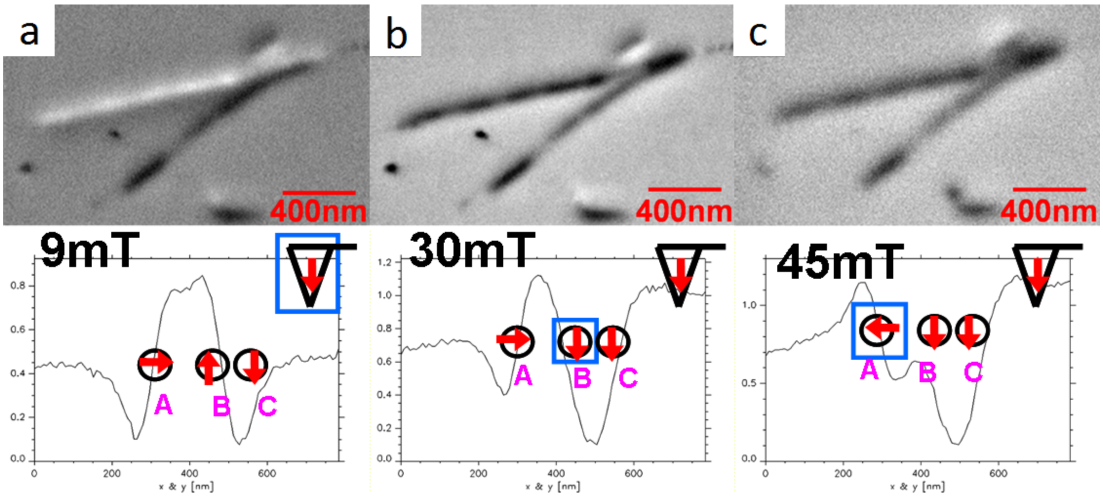

Figure 4.14: Three MFM scans with according line sections (defined in Figure 4.13 (b)) taken at (a) 9 mt, (b) 30 mT and (c) 45 mT [44].

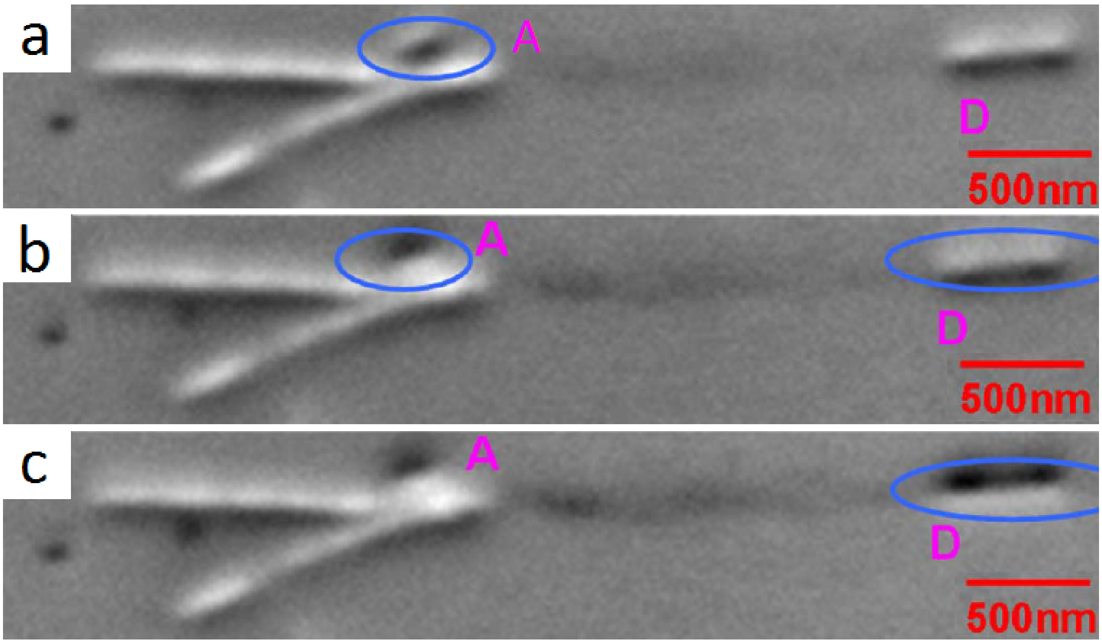

Figure 4.15: hr-MFM scans of four Fe_3C wires, taken at (a) 70 mT, (b) 80 mT and (c) 90 mT. The red circles highlights the switching wire.

applying the in plane fields as close to perpendicular and parallel to wires as possible. The switching of wires **A** and **D** is visualized in Figure 4.15.

The field applied with the IFO is perpendicular to the fast scan axis, from 'top to bottom'. As a result the field is at an angle of ≈ 20° for wire A and ≈ 90° for wire D to the long axis of the wire respectively.

It becomes clear that there is an angular dependence of the switching field. This is best seen in wire A, where the easy, mid-hard and hard axis results are 90, 45 and 160 mT respectively. This is a clear sign that coherent rotation is not the mechanism of magnetization reversal in this particular wire, since that model is 90° symmetric. The data are less clear for the other wires, due to tip sample interaction causing a repeated tip induced switching and problems with IFO operation.

The results are summarized in Table 4.1.

Switching field /mT : angle to axis			
wire	along easy c-axis	along mid-hard a-axis	along hard b-axis
A	90 IFO : ≈ 20	45 PFO : ≈ 0	≈ 160 IFO : ≈ 20
B	29-34 PFO : ≈ 0	no result	no result
C	28 PFO : ≈ 0	30-60 IFO : ≈ 20	≈ 40 IFO : ≈ 20
D	80 IFO : ≈ 0	no result : ≈ 0	≈ 170 IFO : ≈ 0

Table 4.1: Summary of the switching fields measured at certain angles to the corresponding magnetic axes.

The PFO data for wires **B** and **C** further shows that the two wires return to an antiparallel ground state after removing the field which indicates that the stray field of one is sufficient to switch the other. It is always wire **C** that switches after the field is removed, which could be explained by its slightly lower coercivity and/or geometrical considerations. This coupling between the wires means that the measured switching field is not inherent to the wire but is influenced by the environment. That the switching behavior is influenced by the neighbors hints at a localized reversal process, since the field (external field and the superimposed stray field of the neighbor) strong enough to cause switching is only acting at one end of the wire. The most likely candidate for the reversal mechanism is a domain wall propagating through the wire, nucleated from an area exposed to a sufficient field or at a structural inhomogeneity. In theory a coherent rotation of all moments should be possible even in such an anisotropic energy landscape but is unlikely and the dimension of the wire. A nucleation by small volume undergoing coherent rotation has to be considered, with two possible geometries: in the a-c plane via the mid-hard a-axis, or in the b-c plane via the hard b-axis but with support of the shape anisotropy. The two cases lead to an energy barrier of $1.18*10^3 Jm^3$ and $0.88*10^3 Jm^3$ respectively. A rotation in the b-c plane seems to be the easiest path for the magnetization to reverse coherently. The angle dependent data hints at a curling like mechanism for the nucleation, but results are too few and unreliable for a definitive case. Efforts to understand and model the reversal process, with he aid of micro magnetic simulations, in such an orthorhombic system are an ongoing effort.

The notion of a single domain particle is put to the test by the following observation. The switching results for wire D presented in Table 4.1 are not the complete picture.

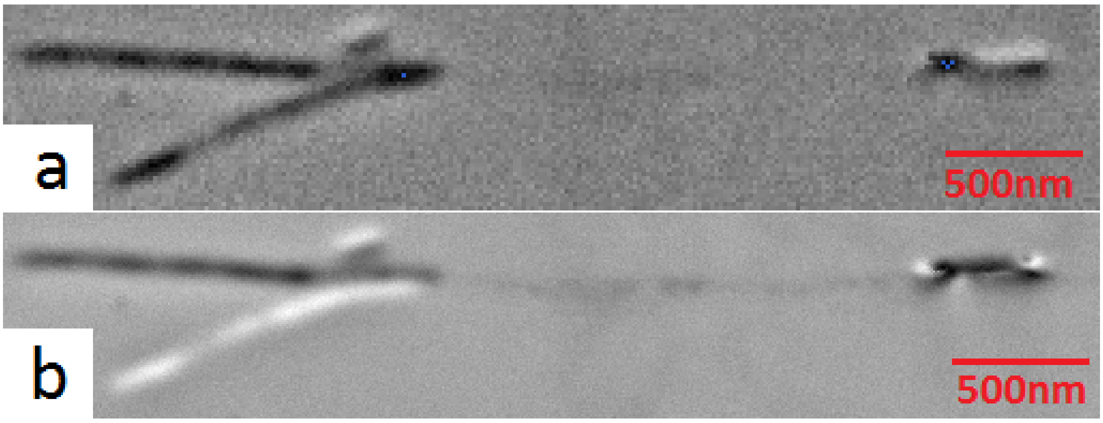

Figure 4.16: hr-MFM image of the four wires. a) With -100 mT applied perpendicular to the wire and b) after removing field.

The two MFM scans shown in Figure 4.16 reveal something unexpected. In (a) Wire D seems to be in a two domain state, and the magnetic configuration leading to the contrast seen in (b) can only be guessed at.

The close ups of wire **D** presented in Figure 4.17 represent a series of measurements. Initially the wire was in the already explained single domain state,

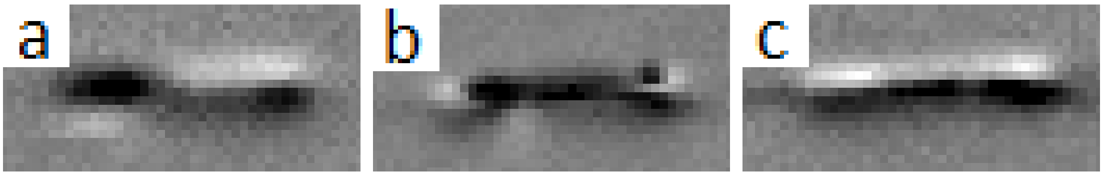

Figure 4.17: Three hr-MFM scans of wire D, taken in series at (a) 78 mT, (b) 0 mT and (c) without changing the setup at 0 mT.

the switching into a 'two domain state' at 78 mT is portrayed in Figure 4.17 (a). After removing the field a new state at 0 mT (Figure 4.17 (b)) is observed, which can not be explained by a classical domain structure. With field still removed, a further scan Figure 4.17 (c) shows the return to a ground state, but the reverse case of the initial magnetization. Since no field was applied after the initial 78 mT, the changing of state at 0 mT between (b) and (c) can either be explained by thermal relaxation into the ground state, or, more likely considering the relatively long timescales involved, the influence of the magnetic tip. Such magnetization arrangements could be intermediate steps in the switching process, a micro magnetic explanation of which is work in progress.

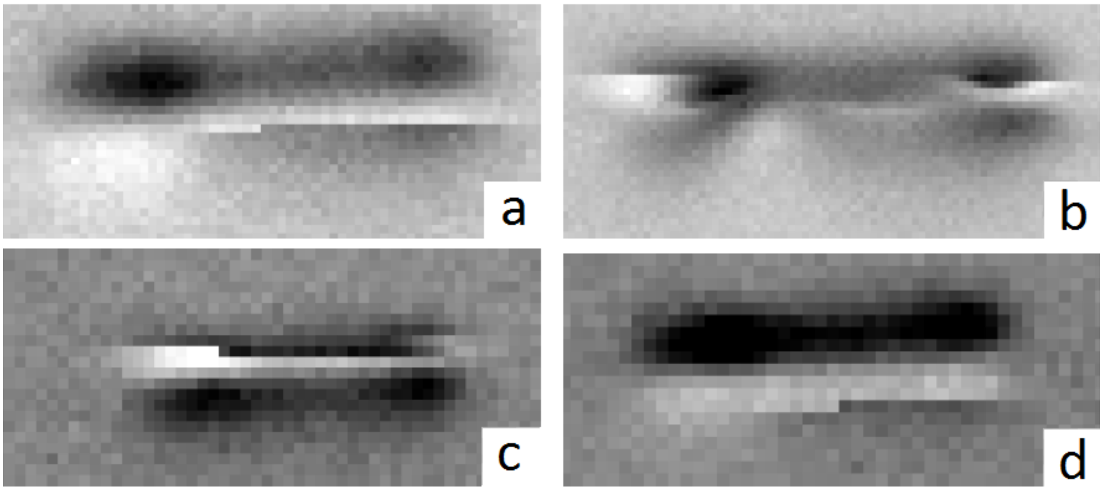

Figure 4.18: Four examples of tip induced changes in the magnetization of wire D.

The influence of the tip can be clearly seen in in Figure 4.18, in all four images the magnetization state of the wire changes abruptly during the scan, seen in the sudden change of contrast within one line or from one scan line to the next. The probability that the tip switched is negligible. The most remarkable contrast observed from wire D is shown in Figure 4.19.

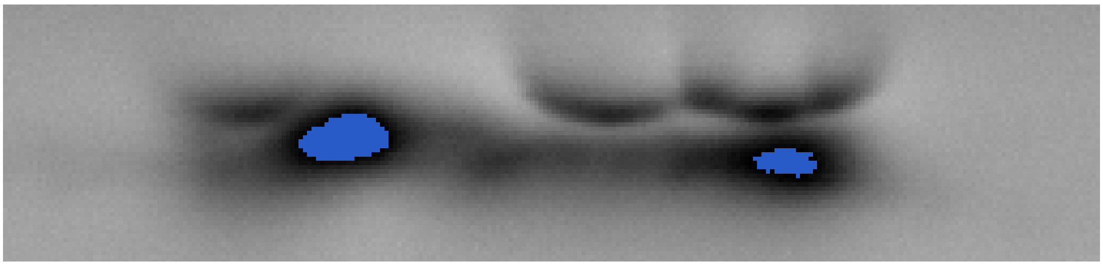

Figure 4.19: hr-MFM contrast of wire D.

A possible explanation for such a contrast could be that wire **D** is not one wire but consists of up to three wires with possibly different orientations of the c-axis. To check this the sample was re-investigated under the SEM.

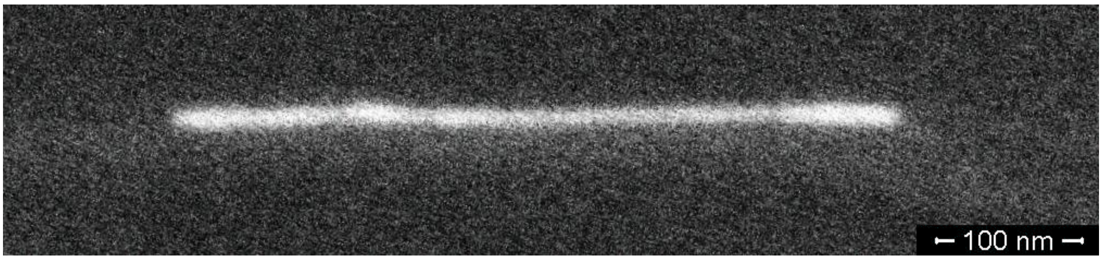

Figure 4.20: SEM-BSED contrast of wire D.

Figure 4.20 shows a close up of wire **D**, taken with the BSED in the SEM. One can see that there are no noticeable gaps within the wire which could explain the MFM contrast presented in Figure 4.19. A more thorough investigation of wire **D** could be achieved in the TEM. Unfortunately, it is not possible to conduct such an experiment on samples on a substrate. Some of the TEM pictures from the wires specially prepared for those observations did reveal some strain within the single crystals. Figure 4.21 shows section of a CNT completely filled with iron carbide. The lighter and darker regions of the filling indicate a divergence from crystal periodicity as can be induced by mechanical stress. It was beyond the scope of this thesis to determine how such strains on the single crystal influence the magnetization arrangement.

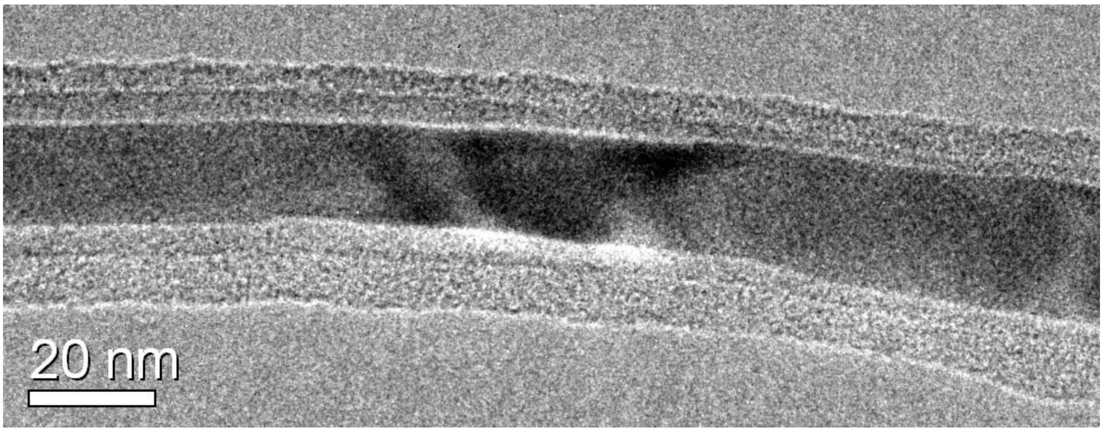

Figure 4.21: TEM image of a single Fe_3C nanowire within a CNT [56]. The darker and lighter areas over the single crystal indicate regions where the crystal periodicity is distorted.

The investigation into explaining the unexpected contrast observed in wire **D** upon applying an external field with the PFO is an ongoing effort.

4.3 Discussion of Nanowires inside Carbon Nanotubes

The results presented in the two parts of this chapter have revealed some important facts about Fe-CNT. Both types, α-Fe and Fe_3C fillings can appear as high quality near cylindrical nanowires, protected by multiple concentric Carbon shells. The main problem is that no method exists to effectively control the shape of the nanowires, and thereby their magnetic properties. A possible approach would be to cut the nanowires into shorter pieces (less than 500 nm) and sort them according to their magnetic properties.

MFM measurements on the two types of encapsulated wires reveal that the remanent magnetization is determined by the competition between shape and magnetocrystalline anisotropy. In α-Fe nanowires the negligible MCA does not contribute to the remanent magnetization direction, also because the crystal orientation relative to the long axis seems to be random, leaving the shape anisotropy dominating. The result is a bi-stable magnetization parallel to the long axis of the wire. Most wires studied for this thesis reversed between 150 mT and 350 mT.

In the case Fe_3C the growth related orientation of the orthorhombic crystal with respect to the long wire axis leads to competition between MCA and SA, resulting in a soft perpendicular magnetization.

The amount of switching events observed for the iron carbide nanowires is too low to draw far reaching conclusions about a possible distribution, but they are clearly lower than that of the α-Fe wires. Here it must be made clear that the switching fields found with the IFO are not very reliable, due to an uncertainty in the positioning.

Both types of wires are thought to switch via a localized reversal mechanism in the form of nucleated domain wall. This is based on the fact that switching can be initiated with only a small section of the wire exposed to a sufficient magnetic field to initiate reversal. The determination of the exact type of reversal mechanism as well as an explanation for the strange contrast found in one Fe_3C nanowire is an ongoing investigation.

The influence of the tip on the switching behavior has potential for exploitation, but for this more reliable and engineerable wires are required. Such artificial arrays of tailored nanowires also have great potential as model system for fundamental physical processes. This idea is the motivation for the second part of the results presented in the next section.

Results and Discussion II - Patterned Elements

An overview of the experimental results on artificial patterns of single domain magnetic elements and a discussion of their significance. A perpendicular magnetic field is purposefully employed with the aim to cause excited states and switch individual elements with the aid of the tip field. Some of the hr-MFM images presented in this chapter were processed by cutting off peaks and troughs of the signal (represented by red and blue contrast respectively) in order to make weaker contrast visible. The findings will be grouped into three sub-sections, simple patterns consisting of single bars and triple junctions thereof, an increasing number of hexagons and finally a large scale square lattice with a focus on edge effects. The discussion for each part will make use of theoretical concepts discussed in the theory chapter.

5.1 Customized Nanowires

Tailoring nanowires allows one to harness their special properties in a controlled and purposeful manner. In the last chapter it was established that the direction of the remanent magnetization of a single domain nanowire is decided by the competition of the relevant anisotropies. For the work presented in this chapter the wires were produced from permalloy (roughly 20% iron and 80% nickel), chosen for its very low magnetocrytalline anisotropy. As a consequence the magnetization direction will be determined solely by the shape anisotropy (SA), favoring the long axis of a wire. The SA acts as an energy barrier between two stable states, comparable to the spin of an electron. Such single domain nanowires can thus be used to simulate Ising spins in certain lattices.

Creating regular arrays of interacting single domain magnets, causes frustration at the intersections. These sites of frustration result in a ground state arrangement which minimizes the stray field emanated from the sample. These 'ice-rules' regulate how the pseudo Ising elements should arrange. All of the possible states of the intersections would be clearly distinguishable in the MFM, although only qualitatively. When applying an external field it is expected that the magnetization of the wires will partly align with the external field, which should diminish the stray field at the intersections. Unfortunately, the hr-MFM is not configured for quantitative measurements.

Large regular arrays are difficult to produce and have already been studied extensively, as by for example Wang et al. [3] and Möller et al. [57], so the author decided to concentrate on border effects. Open ends will always have a charge of ±1, while at the edges double junctions are present, which are expected to be charge neutral (1in1out) but can have an excited state (2in/2out) of ±2. Thus the edges of a lattice will always have magnetic charges, the sign of which depends on the magnetization arrangement within the lattice, giving rise to potential applications as novel logic devices.

The limits of using shape anisotropy to simulate spins (i.e. the validity of the Ising approximation) is of vital importance when wishing to draw conclusions from one experiment about the other environment. Deposited wires will never be perfectly round, the ideal would be an ellipsoid of revolution, which is unattainable due to limitations of the lithography and metal deposition process. Elliptical element work well in isolation, but boarder effects would quickly diminish any theoretical advantages as soon as interconnection is required. In the following experiments rectangular wires were used, connected at the intersections to warrant exchange coupling. It could be argued that the the notion of single domain does no longer apply, due to the increased effective size. The motivation for the following experiments was the fact that despite the connection, each element should continue to act as a single domain magnet, with magnetization of the connecting squares indicating the arrangement of the surrounding elements. The results will be split into three sections, with the studied patterns growing in size and complexity.

The electron beam lithography (EBL) process was conducted with the help of Kamil Lipert and the metal deposition was undertaken by Joachim Schuhmann. The quality of the deposited nanoelements can be judged from the AFM images (Figure 5.1) taken as part of the lift-mode MFM data (presented in Figure 5.6)

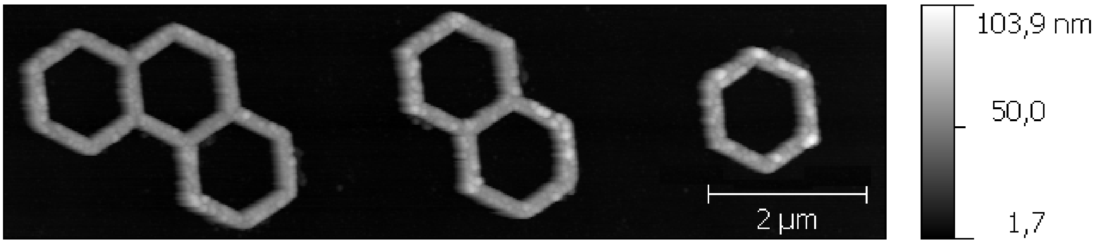

Figure 5.1: AFM image of the three smallest patterns. One can notice that some of the irregularities on the elements are as high as 50nm, the height of the elements themselves.

Figure 5.1 shows the three smallest elements h-3, h-2 and h-1. The hight information extracted from the AFM scan reveals that features are present which are over 50nm higher than the anticipated total hight of 50nm. Such irregularities not only limit the quality of the hr-MFM scans by forcing a greater separation but can also influence the magnetic properties. Such sites can act as nucleation or pinning sites altering the the magnetic hardness and hence their value as tools to simulate Ising spins.

5.2 Groups of Ising Spin Simulating Magnetic Bars

Initially various patterns of individual bars were studied to test the quality of the Ising assumption for the bar elements. Dimensions were chosen as a compromise between making the EBL process reliable, get sufficient signal strength and a good number of elements into the scan area of the MFM, all within the single domain limit. The bars have a length of 600nm, a width of 125nm are 50nm high. An increasing number of triple junctions is used to test the validity of the 'Ice-rules'. In the ground state each triple junction is either forced into either a 2in1out or a 1in2out state. An excited state would be a 3in or 3out.

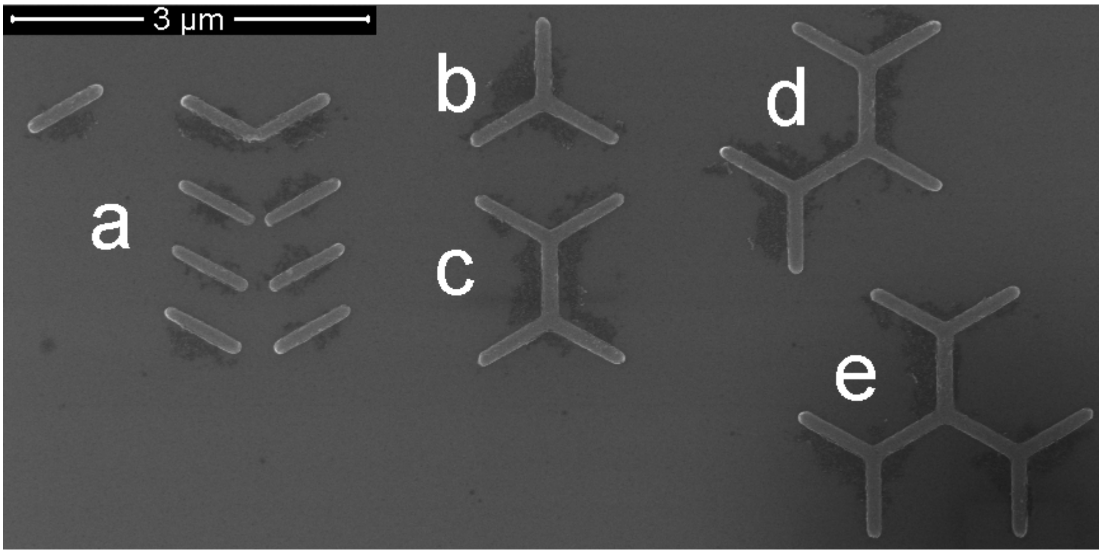

Figure 5.2: SEM overview of five groups of elements.

Figure 5.2 shows an overview of the first set of elements. Group (a) consists of individual bars which are brought gradually closer, until two of them touch. The angle of the bars is 30° to the horizontal, resembling their arrangement in the triple junctions and hexagons later on. Group (b) is a single triple junction which introduced frustration by forcing the individual magnetizations to arrange according to the ice-rules. Group (c) consists of two triple junctions connected by a shared element, (d) of three triple junctions and (e) of four triple junctions.

The magnetic signal of the patterns shown in Figure 5.2 is presented in the hr-MFM scan presented in Figure 5.3. All individual elements (group (a) show dipolar contrast, as soon as the two bars are in contact (exchange coupled) the combined element shows a single dipolar contrast. Before joining, the contrast orientation of the dipoles is random indicating that at least in the virgin case the stray field interactions between neighboring elements seems to be of no significance. The patterns b-e show contrast at the junctions as expected from the 'ice-rules', which dictate a value of +1 for 2in1out and -1 for 1in2out. The 'open ends' show the same intensity of contrast, which indicates the same magnetic charge of ±1.

Figure 5.4 shows what happens when applying an out of plane external

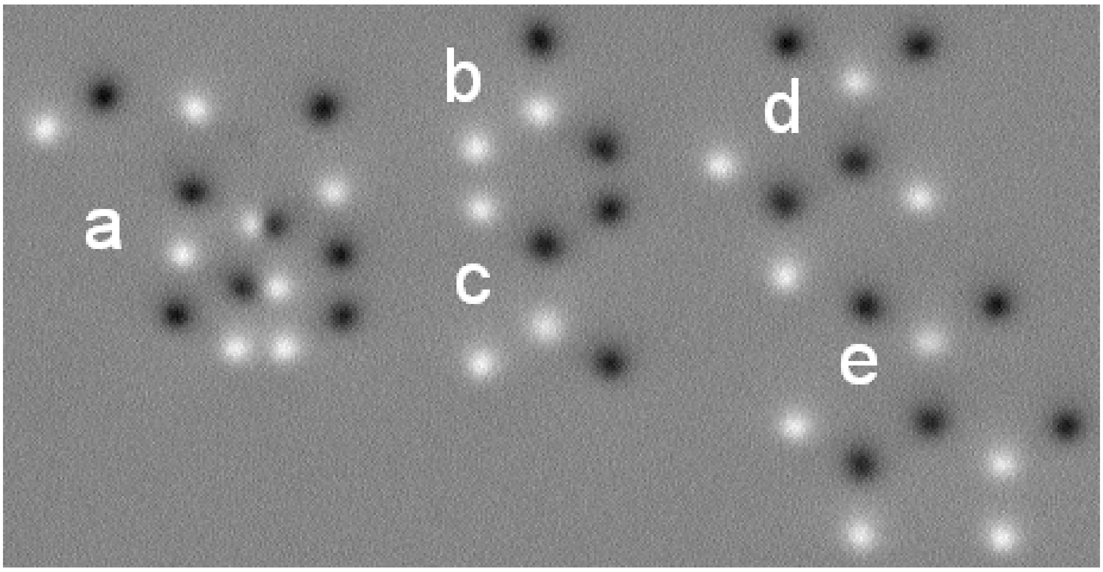

Figure 5.3: hr-MFM overview of the same area as Figure 5.2, showing the stray field emanating from the ends of the wires.

magnetic field with the PFO. In Figure 5.4 (a) a field of 150 mT causes an out of plane magnetization component to appear along the elements. The magnetic signal at the ends of the elements has not changed qualitatively, indicating that the tip magnetization was already parallel to the applied field and that no switching of individual elements has occurred. No quantitative information about the signal strength of the emanating stray field can be extracted from the data. The case is quite different in Figure 5.4 (b) which shows the elements at 0 mT but after having been exposed to 400 mT. It is clear that the out of plane magnetization component disappears upon removing the external field, as would be expected for the shape anisotropy governed remanent magnetization. When looking at the ends of the elements one can see that multiple bars have switched. A surprising result can be observed in pattern **a**: the double bar (labeled **a1** in Figure 5.4(b)) shows positive contrast at the junction. Such a head to head arrangement is not favorable energetically and indicates a pinning, showing that the kinks could be a weak spot in the following investigations. The fact that the elements switch at all when exposed to a perpendicular field has two possible explanations. Firstly, the field alignment and geometry of the sample could be perfect in which case the

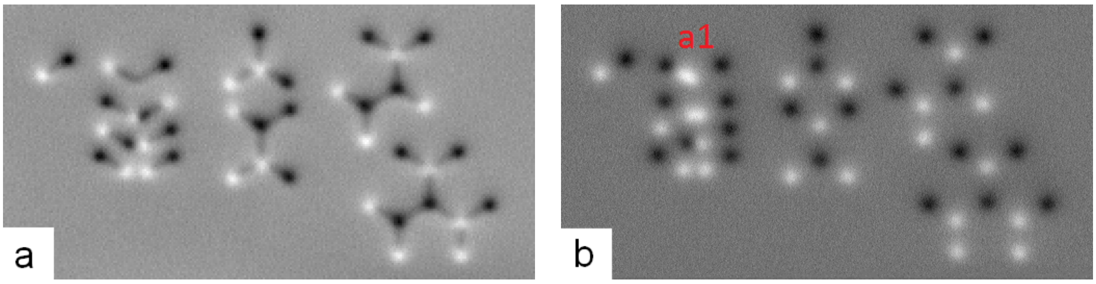

Figure 5.4: (a) hr-MFM image of the patterns with an external field of 150 mT applied. An out of plane component can be seen along the elements. (b) hr-MFM image of the patterns at 0 mT after an external field of 400 mT was applied.

external field would completely magnetize the sample out of plane, with thermal fluctuations deciding in which direction the magnetization will point upon removing the field. The second scenario would be that there is a finite angle between the field and the sample normal meaning that there would always be an in-plane component, causing switching in a preferred direction. Viewing the arrangement in Figure 5.4 one can clearly see a large scale order, the positive contrast tends to be at the bottom end of the scans while the negative at the top. Since the scan direction and orientation hast remained constant throughout, this indicates that indeed there is significant angle between the sample plane normal and external field. This angle results in a sufficient in-plane (y-direction) component to overcome the shape anisotropy as seen in pattern **a**.

5.3 Hexagonal Elements

Patterns consisting of an increasing number of hexagons were produced to test the 'Ice rules' in a more complex environment. A large scale array of hexagons is referred to as honeycomb lattice which is equivalent to a lattice of triple junctions. Again, each triple junction can be in a 2in1out/1in2out ground state or a 3in/3out excited state. The double junctions can be in 1in1out state or an excited 2in or 2out state. All these states are clearly distinguishable in the MFM.

The hexagons consist of the same bar elements as used in the previous section: length 600nm, width 125nm and height 50nm. Figure 5.5 is an SEM image of the seven patterns studied in this section. Starting of the right they consist of one, two, three, four, five, seven and eight hexagons (referred to as 1-h, 2-h etc).

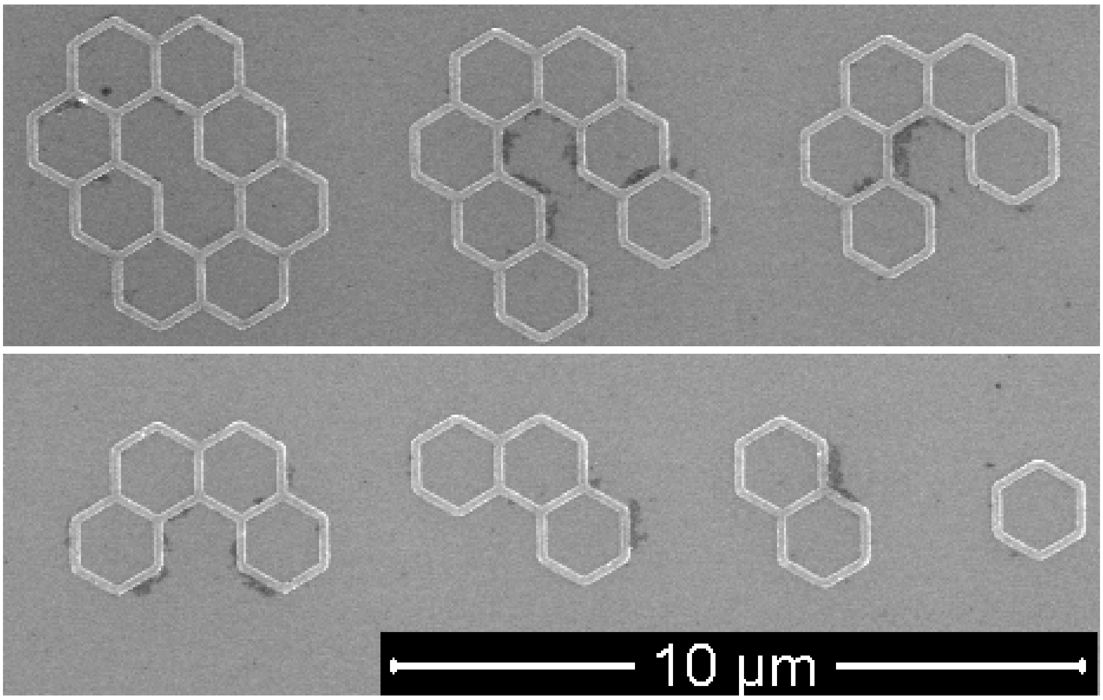

Figure 5.5: SEM overview of seven patterns consisting of an increasing number of hexagons.

A single hexagon allows for the dipoles to arrange in a circle, with no resulting stray field. The introduction of a second hexagon, sharing one bar element or side, introduces frustration at the two triple junctions. Here the 'ice-rules' apply once more, with the ground state of the whole system being a 2in1out state at one triple junction and a 1in2out on the other. This equals a magnetic charge of ±1 and is therefore indistinguishable from an isolated bar element.

Figure 5.6 shows four MFM scans taken in the lift-mode without an applied field. Figure 5.6 (a) shows the expected ground state result. The single hexagon shows no magnetic signal, the 2-h a dipole over the shared element and the 3-h two dipoles arranged to minimize interaction. Surprisingly, also other zero field arrangements were found despite not being exposed to an external field (Figure 5.6 (b),(c) and (d)). An explanation for this effect is the fact that the spontaneous

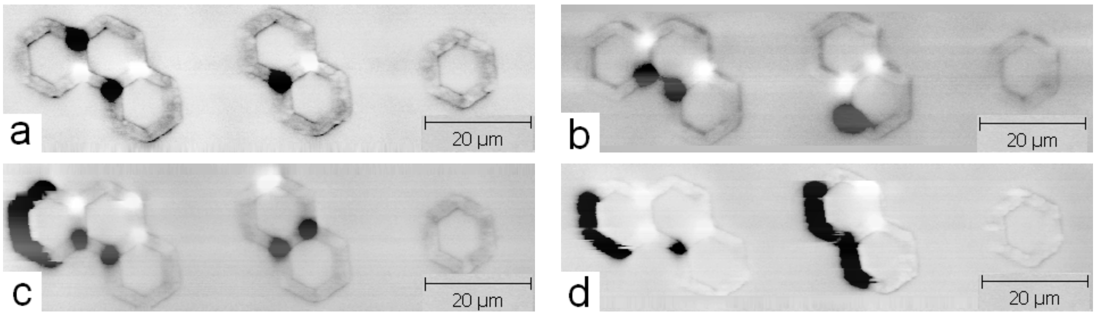

Figure 5.6: Four lift mode MFM scans (phase shift) of the first three hexagon groups. The single hexagon shows no magnetic signal. The 2-h and 3-h show four different magnetization states. (a) is the overall ground state. The elongated negative contrast in the other three images (b-d) represents an out of plane magnetization of the according element.

magnetization during cooling (after the production process) does not necessarily have to occur simultaneously for each of the individual bar elements. This can lead to additional frustrations. The dipolar interactions are not strong enough to switch neighboring elements, leading to a freezing into a 'non-ground state'. Another explanation, especially for the extended negative contrast observed in Figure 5.6 (c) and (d) is that of an interaction with the magnetic tip. During lift mode scans the tip comes very close to the patterns, possibly switching soft elements. To avoid this effect and apply magnetic fields the sample was transfered to the hr-MFM which uses a low moment high resolution tip.

On first sight two differences between Figures 5.7 and 5.6 are obvious. Firstly, there is no hint of the topography in the hr-MFM pictures, a result of the non-contact measurement mode and careful adjustment of the sample bias to avoid EMF signal. As a second point one has to notice the higher sensitivity and resolution, even weak magnetic contrast aside from the expected sources is visible which is only barely hinted at in the lift-mode images. To further explore this point Figure 5.8 shows an image of the individual hexagon.

In the absence of the strong magnetic signals expected from frustrated junctions or the break down of the Ising properties discussed above, weaker and more confined sources of stray field can be clearly identified in Figure 5.8.

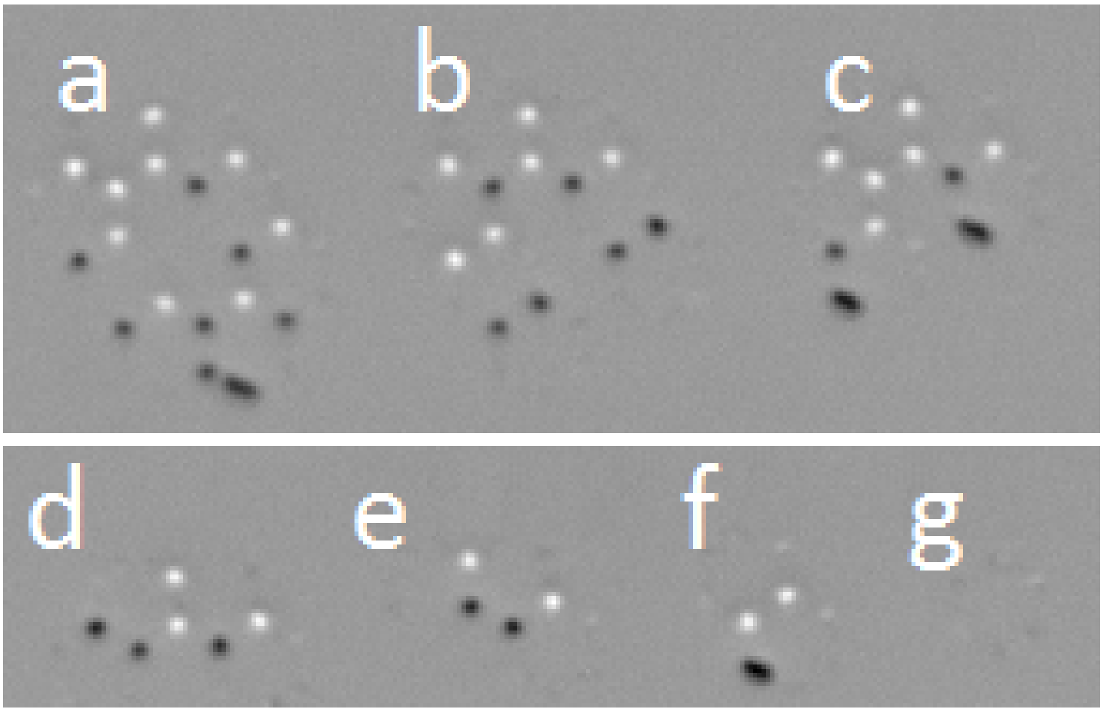

Figure 5.7: hr-MFM image of the complete set of seven hexagonal patterns (a-g).

Figure 5.7 reveals that not all patterns of hexagons are in the ground state, some are in an higher energy configuration. Here the author would like to introduce two different kinds of higher energy configuration (HEC). A pattern with more than two intersections, resulting in more than two effective dipoles, can arrange in a way so as to minimize the dipole interaction, which would be the ground state (for example the 3-h in Figure 5.6(a)). If two dipoles are arranged in another way this would be HEC1 (Figure 5.6(b)). The third case (HEC2) is that when the Ising behavior breaks down and an element (or junction) between two elements (without frustration) features magnetic contrast. All cases are visible in Figure 5.7: (b),(d) and (e) are in HEC1; (a),(c) and (f) in HEC2. Only (g) is in the GS.

Upon applying an out of plane magnetic field one initially observes the switching of the MFM tip, which occurred at 25 mT or below, then an out of plane component to the magnetization of the hexagons appears, followed by a rearranging

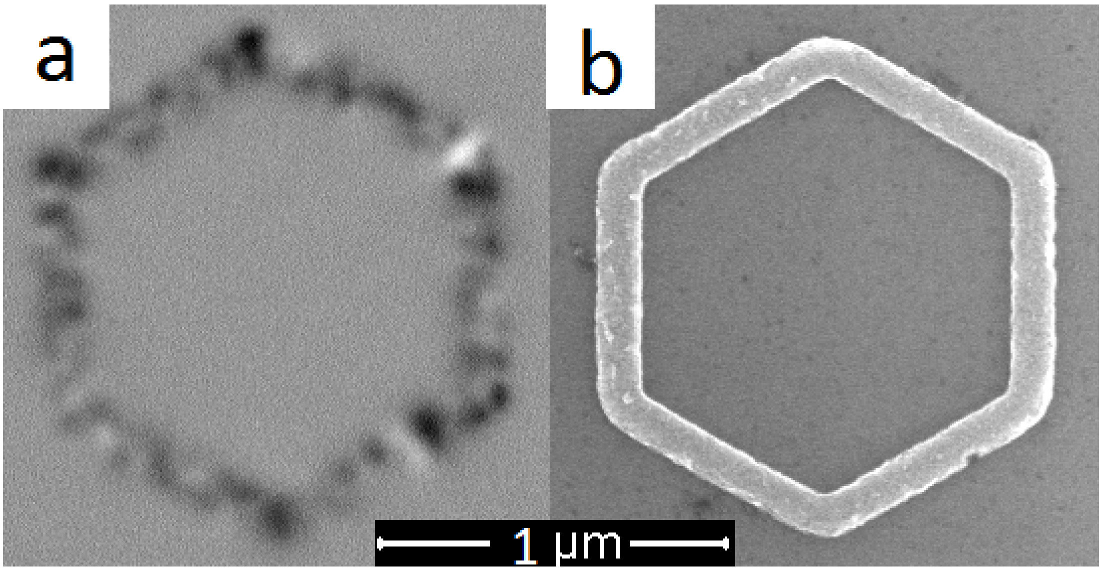

Figure 5.8: (a) hr-MFM image of a single hexagon. Magnetic contrast is clearly visible along the elements, with two slightly stronger signals which appear like domain walls. (b) SEM image of the same hexagon.

or switching at higher fields. Figure 5.9 shows the elements with an applied field of (a) 75 and (b) 200 mT.

The rearrangement can be seen more clearly when removing the external field, causing the out of plane component to disappear. When comparing Figure 5.7 with Figure 5.10 below, one can clearly see that the magnetic configuration has changed.

All patterns except (g) have altered their configuration. (a) is in a different HEC2, (b) changed from a HEC1 to an HEC2, (c) is in a different HEC2, (d) changed from a HEC1 to an HEC2, (e) changed from a HEC1 to the GS, (f) changed from HEC2 to the GS and (g) remained in the GS. The most noticeable observation is that no more HEC1 states are observed. An explanation for this would be that the external magnetic field was sufficient to overcome the energy barrier posed by switching one of the connecting elements or an outer ring of five elements. In pattern (e) most likely the element at the boundary between the central hexagon and the bottom right one has switched. The cases of (b) and

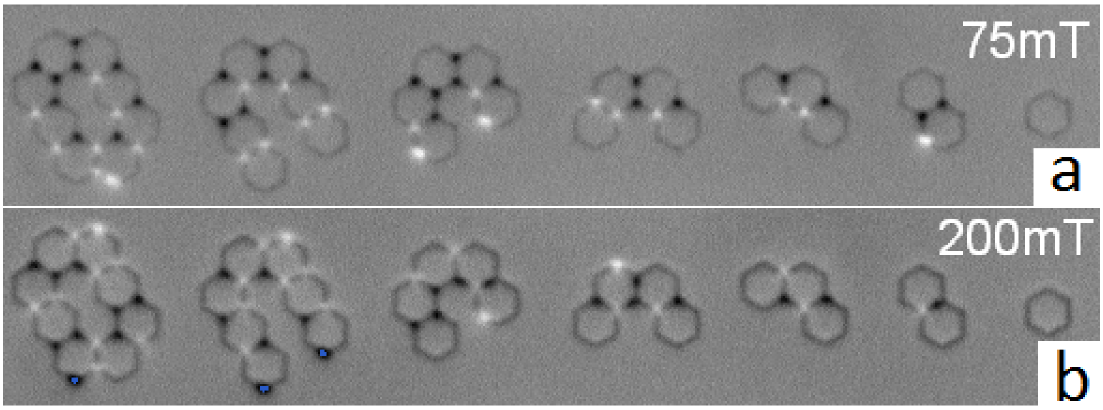

Figure 5.9: (a) hr-MFM image of the set of elements with an applied field of 75 mT. The strong stray field sources at the frustration and HEC2 sites remains unaltered, a slight out of plane (dark) contrast is observed over all magnetic structures. (b) shows the same set at 200 mT. The out of plane component is stronger, but more importantly a rearranging of the effective poles and HEC2 sites has occurred.

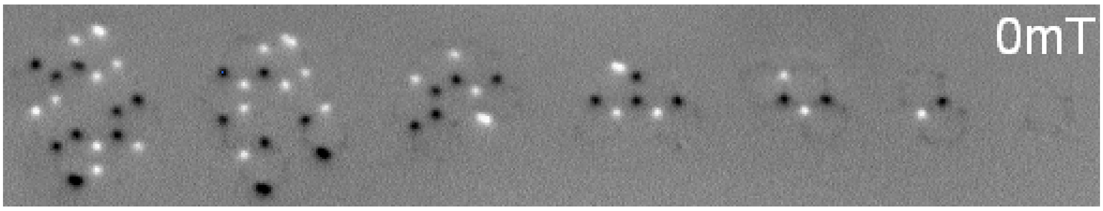

Figure 5.10: hr-MFM image of the complete set of hexagonal patterns at 0 mT after applying 200 mT.

(d) are also interesting, they were initially in a HEC1 state and switched into a HEC2 state. This further strengthens the assumption that the poor quality of the elements seen from the AFM images in Figure 5.1, is responsible for weakened shape anisotropy, leading to bad Ising spin behavior. Further, the notion of a strong in-plane component is supported by the final arrangement of pattern **a** and **b** as seen in the comparison between Figures 5.10 and 5.8

5.4 Edge Effects in Large Arrays

Moving on from the individual elements, the author investigated a larger array of elements. Unfortunately, the production of the hexagonal array was not successful, but a few of the quadratic arrays yielded sections suitable for MFM measurments. In the square case there no triple junctions but quadruple junctions instead. For each quadruple junction there are three states; 2in2out should result in no net flux emerging from the junction, 3in1out and 1in3out result in a charge of ± 2, while 4in and 4out yield ± 4. The three states should be easily distinguishable under the MFM. Since the focus lies on edge effects one also has to consider T-shaped triple junctions, at the edges, and 90° double junctions at the corners.

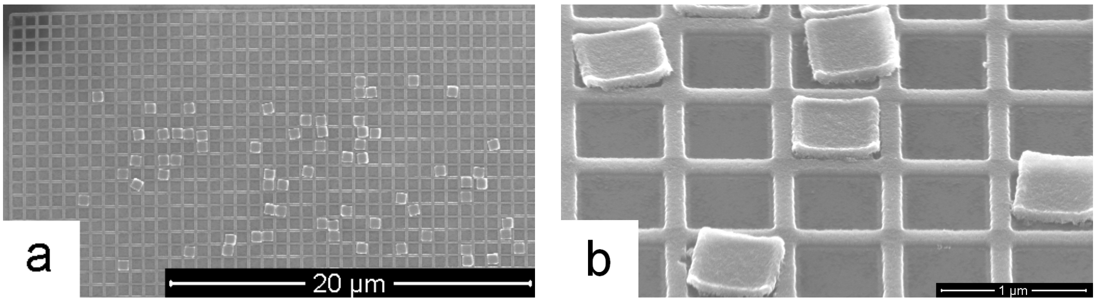

Figure 5.11: (a) SEM image of the extended array, the lift off procedure was only partially successful. The top five rows of this area are investigated with the hr-MFM. (b) Zoomed SEM of an area where the lift of did not work properly, taken at an angle to get an idea of the height differences.

Figure 5.11 shows SEM images of the array studied. The lift-off procedure was only partially successful leaving behind some of the 'cut-out' squares as seen in Figure5.11 (b), such squares would make it impossible to perform hr-MFM which requires very flat samples. In some areas the lift-off worked better, one large area is shown in the top left of Figure 5.11 (a). This area is ideal for MFM studies since it is large enough to get a good sample, of rectangular shape, and in a corner, allowing one to study edge effects.

Figure 5.12 is an hr-MFM scan of a large section of five rows by 40 columns amounting to (4*39) 156 quadruple junctions, 43 triple junctions at the edges and one double junction at the corner. The circle in the bottom right corner indicates that the tip magnetization is pointing up. The sample was exposed to the maximum applicable field of + 600 mT before the scan. The corner (double

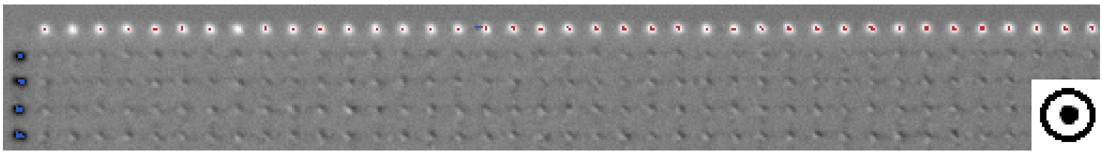

Figure 5.12: hr-MFM image of the top section of the array (five rows by 40 columns), after the sample was magnetized to positive saturation. The circle in the bottom right corner indicates the direction of tip magnetization.

junction) is not visible in the scan suggesting a 1in1out arrangement (=0). The triple junctionss along the top edge show a positive contrast, which has to be 1in2out (+1), while those on the side edge have negative contrast (2in1out (-1). The quadruple junctions are only bearly visible and that only after cutting off the maxima and minima of the edge signals (red and blue areas respectively) indicating the expected 2in2out ground state. A repeated contrast is visible over the quadruple junctions, observed in more detail in Figure 5.13.

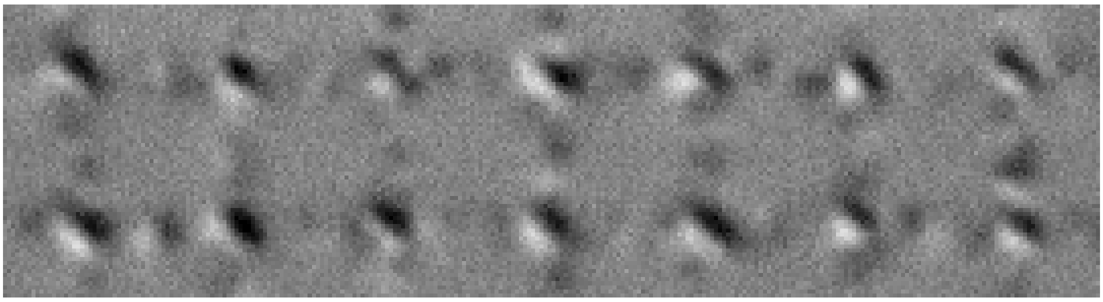

Figure 5.13: hr-MFM image of fourteen quadruple junctions.

Fourteen quadruple junctions are shown in Figure 5.13, with the diagonal contrast clearly visible across the intersection, which could either be a domain wall or a weak effective magnetization. The first case would occur if the dipoles of the wires opposite each other enter the quadruple junction head to head and tail to tail forcing the two flux paths to run antiparallel with a domain wall in between. If both dipoles enter head to tail, the paths would be parallel leading to an effective magnetization. Considering the scale and regularity of magnetization pattern, only the second case can work. Some magnetic contrast can also be seen on the bar elements themselves, most likely due to structural irregularities.

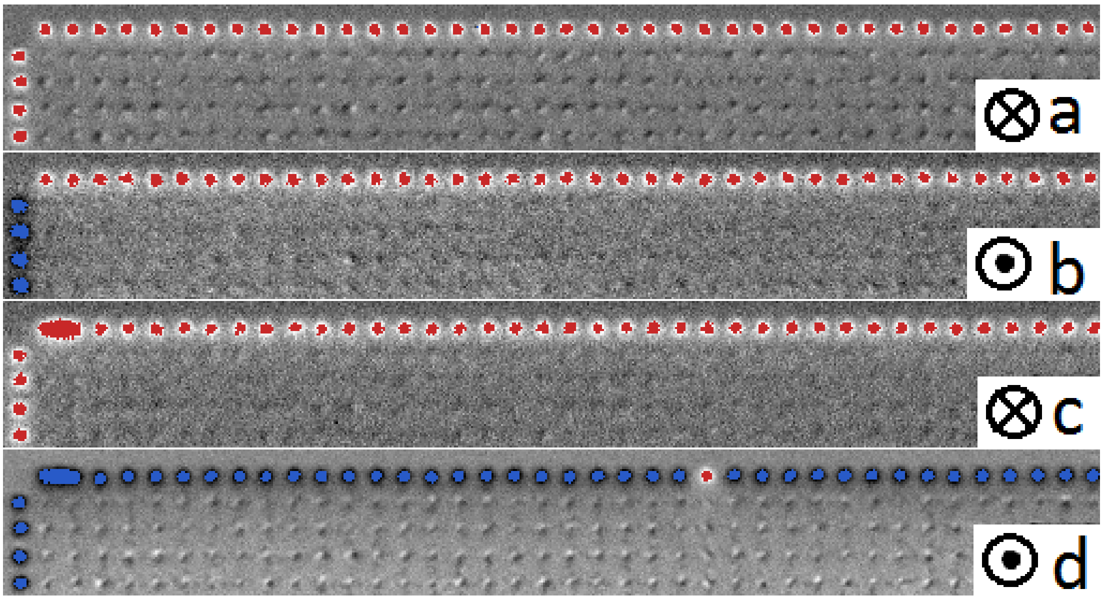

Figure 5.14: hr-MFM scanns after applying consecutively (tip always parallel to applied field): (a) -400 mT, (b) +300 mT, (c) -200 mT and (d) +100 mT. The direction of the tip magnetization is indicated in the bottom right corner.

Upon applying alternatingly decreasing magnetic fields, the field range at which switching occurs can be found. The results of the coarse search are displayed in Figure 5.14. It is important to mention that the tip magnetization is soft compared to the switching fields of the elements involved, it is therefore always oriented parallel to the currently applied field. Comparing Figure 5.12 and Figure 5.14 (a) one can see that the side edge triple junctions retained their original orientation (the tip magnetization has reversed which causes an inversion of contrast) while the top edge triple junctions have reversed their signal, achieved by reversing the magnetization direction of the columns. (b) shows the same contrast as Figure 5.12, so again all the columns have switched. In (c) a breakdown of the Ising assumption for the individual elements can be observed, the element combining the first and second triple junction on the top from the left is continuously magnetized out of plane, antiparallel to the tip. This defect is stable upon removing the field and even applying an opposite field of 100 mT (d), just as most of the other magnetizations, now appearing as negative contrast because the tip has switched. The exception is the 26th column from the left, which has switched magnetization, clearly seen by the positive contrast in the corresponding triple junction.

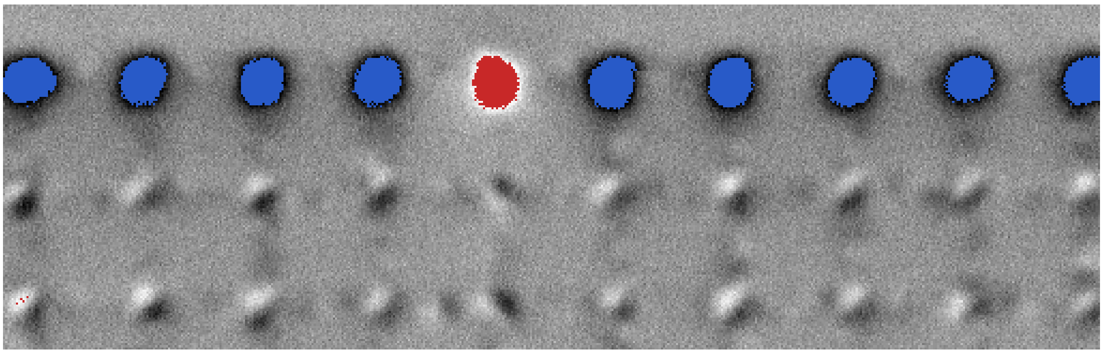

Figure 5.15: hrMFM image of 10 columns.

A close up of the corresponding section from Figure 5.12 (d) is presented in Figure 5.15. One can clearly identify that the contrast over the quadruple junctions has rotated by 90°, this can be explained by a switching of the corresponding column.

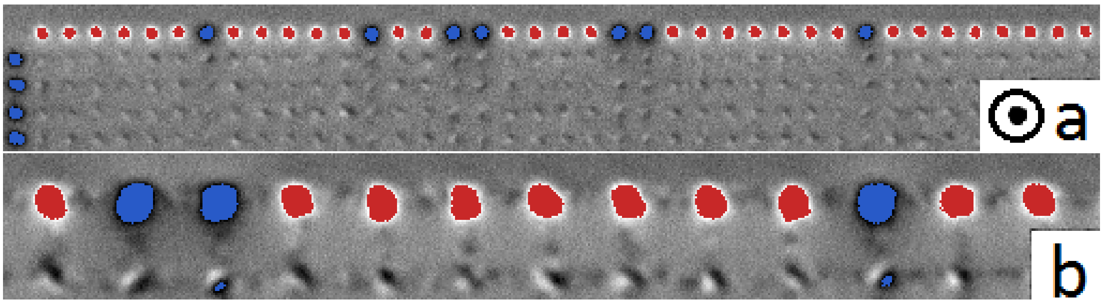

Figure 5.16: (a) hr-MFM scan after applying +150 mT. (b) Close up of two rows by 13 columns.

The scene after applying +150 mT is displayed in Figure 5.16, (a) is an overview of the whole scene of interest where 32 out of 39 triple junctions have reversed their signal, indicating that the corresponding columns have switched.

A section of 13 quadruple junctions with the corresponding triple junctions is presented in (b) where ten of the switched triple junctions are visible. This also clearly seen in the contrast across the corresponding quadruple junctions. This shows once more that the entire column has to switch when the triple junction switches, otherwise a higher energy state would have to emerge at one of the quadruple junctions.

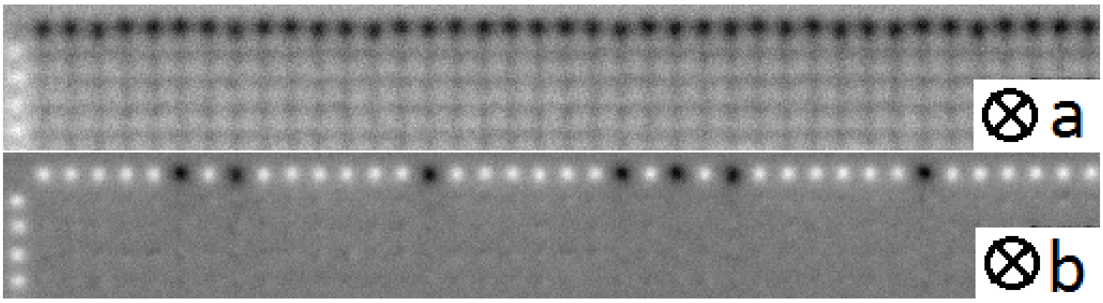

Figure 5.17: hr-MFM overview scan (a) with -100 mT applied, (b) after having applied -150 mT.

The effects of applying an opposite magnetic field are presented in Figure 5.17. After saturation in a positive field, with -100 mT applied (a) the elements are visible due to the induced out of plane component. The large scale arrangement is in the ground state. After having applied -150 mT all but seven columns have switched. One can only speculate if it is a coincidence that once more 32 columns have switched at an applied field of 150 mT. After having applied -200 mT all the rows have switched, further the defect between column two and three has reappeared (Figure 5.18). This magnetic defect does not affect the magnetization structure of the surrounding elements, therefore it does not represent an excited magnetic state but must have its origin in a structural defect.

The magnetization reversal of the entire grid occurs in the following stages. The magnetization of the horizontal elements (rows) did not change over the course of this study, solidifying the assumption that the sample was slanted, mainly in the y-direction. The columns start switching at around 100 mT, where it is important to note that always the entire column has reversed. At 200mT the reversal of the columns is complete, and the defect in the top element connecting columns two and three appears.

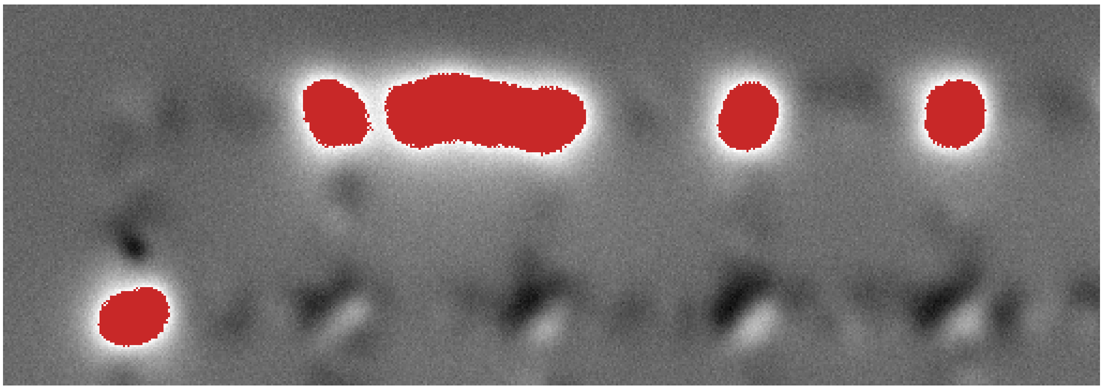

Figure 5.18: hr-MFM close up of the defect in the top left corner.

After reviewing the results obtained by the hr-MFM under applied fields, the foremost observation is that no higher energy states could be found, aside from structural defects. The main drawback is that a field applied perpendicular to the magnetized bars does not really influence energetics of the excited states in the same way as a parallel field would. In all three types of patterns studied, out of plane magnetizations were found where they should not be meaning that the Ising assumption for these particular single domain magnets is not valid. This is probably due to a poor quality of the wires, greatly reducing the shape anisotropy and hence the hardness. A significant in-plane field component is caused by slanted mounting of the sample.

No influence of the tip was observed, not only were no excited states or 'monopoles' created but not even the switching of a single wire element to change a HEC1 into a ground state occurred. The most likely explanation is the much larger volume of the magnetic wires studied in this section compared to the encapsulated nanowires from the last section. For the increased dimensions the weak and very high gradient field has almost no significance when compared to the homogeneous external field.

No information was gained about the possible switching mechanism occurring in the tailored nanowires. Considering the dimensions and low quality of the wire a curling reversal of a small volume followed by a propagating domain wall is again the most likely candidate.

5.5 Comparison of all Nanowires and Conclusions

Comparing the results of this chapter the findings on the encapsulated wires one notices the importance of the shape of the wires. The CNT act as a mold for forming close to perfectly cylindrical nanowires as well as protecting them from deterioration. The quality of the tailored nanowires on the other hand is subject to the limits of the production process.

Encapsulated wires can come close to the ideal shape used in most simulations, very long with a constant diameter and rounded ends. In practice it is rare to find such a perfect wire with the added difficulty of then having to place it in a manner enabling one to study it. The approach employed in this work was to spread the wires randomly over a patterned surface, look for suitable wires with the SEM and then study them with the MFM, a procedure which is very time consuming. For α-Fe a second approach using embedded wires, allows one to study more wires at once, but no information can be extracted about the diameter, length or distance from the surface. The combination of both approaches, a large number of 'anonymous' switching field values from one, and a few switching fields with corresponding wire dimensions known, would have given a good picture. However, the difficulties connected with the IFO operation, in concert with the low maximum field of 240 mT, meant that only a single 'side view' switching event was observed in α-Fe nanowires, in a rather small and asymmetric specimen.

The individual switching studies worked far better for the encapsulated Fe_3C nanowires, since their switching field is an order of magnitude lower and the system is orthorhombic, meaning that the much more precise and reliable PFO could be employed for half of the switching results. It was during these PFO studies that the inexplicable contrasts emerged in one of the wires. The limits of SEM resolution were reached in the attempt see if the wire was fractured. If the wire is a single crystal it could still be subject to deformation as shown for a different wire under the TEM, but it remains to be investigated how this could influence the magnetization arrangement in such way. A possible approach would be to employ electron holography in the TEM while using a micro manipulator to excert forces on the wire.

In the experiments with the pattered elements the hr-MFM proved a valuable tool for precisely determining the magnetization state of a large number of wire elements. The hr-MFM is sensitive enough to resolve contrast apart from the expected one at the poles of the wires enabling one to investigate the structural quality. The fundamental properties of patterned elements in arrangements of increasing size were studied, with the edges identified as possible read-out sites for the magnetization arrangement of entire rows or columns. Some basic switching behavior was observed with the PFO, although it was mainly due to the in plane component which originated from the samples slanted mounting. The IFO had deteriorated beyond practicality at his stage. Initially, there was hope to find some excited states not caused by edge effects or defects, and even create one with the aid of the tip field. The last point was inspired by the tip induced switching described for the encapsulated nanowires. The first goal was achieved when contrast appeared at unfrustrated interconnections, but this is only a sign of the poor wire quality. The wire elements selected for this study proved to be not 'Ising' enough, as demonstrated by the breakdown of single domain behavior. The choice of material is not the problem, permalloy is ideal due to its very low MCA and high moment, but rather the fault should be sought in the shape of the wires. By virtue of the production technique it is impossible to create round wires. This reduction of symmetry significantly diminishes the shape anisotropy responsible for creating hard single domain magnets.

The dimensions of 600 nm*125 nm*50 nm were chosen as a compromise between reliable production, sufficient signal and that enough junctions fit into the scan area of the hr-MFM to get good statistics. A possible improvement would be to optimize the wire dimensions. To create more symmetric wires would strain the limits of the EBL and metal deposition process, a roughly cuboid shape could be achieved, but would be hard at the required dimensions. An open question is also how the exchange coupling at the intersections influences the single domain character, because in reality it is a multi domain object with the individual domains restricted to areas imposed by geometry.

There definitely is vast potential in magnetic nanowires, though they need to be precisely tailored for each application. Throughout the experimental work the hr-MFM proved to be a valuable tool, although the preparation for measurements proved rather time consuming, as one has to wait several hours for the vacuum to form. Especially for the encapsulated wires it has a major advantage over other magnetic imaging techniques such as Kerr microscopy, since it directly measures field gradients. Further, the PFO proved very effective, especially the application of a field while scanning turned out to be invaluable to pinpoint switching fields to within a couple of mT. The IFO on the other hand proved to be very cumbersome and many days were invested into getting results which are not fully trustworthy. A heating stage is still in development by the supplying company which would have made it possible to heat iron carbide wires up to their Curie temperatures. On the route there it might have been possible to observe a switching from transverse to parallel magnetization, since the MCA diminishes faster with temperature than the saturation magnetization responsible for the magnitude of the shape anisotropy.

The physics of nanomagnetism is a fascinating field of research which has considerably advanced technology and will continue to do so. Cheap and high performance hard magnets are essential for advancing the trend towards renewable energies, as the they are essential components of converting kinetic energy into electricity and vice versa.

Summary

This thesis describes a series of experiments designed to gain insight into the role of anisotropies in deciding the magnetic properties of single domain single crystal nanowires. The main experimental tool employed was a MFM with the option of applying magnetic fields which allows one to study the remanent magnetization as well as the switching behavior. The crucial link to the morphology and crystal orientation is supplied by SEM and TEM investigations.

Single domain magnets are a great toolkit which can be applied to investigate several fundamental and applied concepts. Further, single domain nanomagnets can be employed to create model systems by simulating Ising spins. This thesis covered two distinct types of nanowires, the near cylindrical wires found inside carbon nanotubes and custom made elements, each possessing significant advantages and drawbacks.

CVD grown iron filled carbon nanotubes, were investigated in two variants consisting of either a single crystal α-Fe or Fe_3C filling the hollow of a CNT. Both materials can form cylindrical wires of more than a micrometer length and the diameter of the hollow of the CNT. They are ferromagnetic at room temperature, but otherwise their magnetic behavior is very different. In both cases, the magnetic wires are shielded by protecting carbon layers. This results in a wear resistance and protection against oxidation of the magnetic filling which renders both materials exploitable for long lasting applications. The CNT also protects the environment from potentially toxic filling as required in biological environments.

The low magnetocrystalline anisotropy of α-Fe means that the magnetization of such nanowires is governed by the shape anisotropy resulting in a stable magnetization along the long wire axis. In the case of a magnetization paral-

lel to the long axis the MFM reveals an extended dipole over the wire length. For possible applications of ensembles it is necessary to determine the individual switching field of a large variety of nanowires. Hence, a method was applied which allows detecting the switching field of 58 iron nanowires from the same batch. The switching field distribution for such wires shows a large variation with most wires switching between 150 mT and 350 mT, undesirable for applications, yet expected for the random growth process. These values lie beneath what would be expected for ideal wires, since defects can act as nucleation sites in a thermally activated curling of a small nucleation volume followed by a domain wall propagating thorough the rest of the wire. The results on the α-Fe nanowires revealed the importance of the MFM tip's influence. The high gradient tip field can initiate a nucleation by locally warranting a sufficient switching field.

For Fe_3C the case is different, it features a strong magnetocrystalline anisotropy dominating over the shape anisotropy. The result is that the remanent magnetization is determined by the orientation of the orthogonal single crystal relative to the long axis of the wire. Due to the rigid constriction imposed by the CNT hollow, the b-axis tends to form along the long axis, causing the magnetic easy c-axis to be perpendicular to the shape anisotropy. The resulting competition leads to a weak magnetization perpendicular to the long axis. In the MFM this is revealed as extended contrast parallel to the wire's long axis, either a single signal over the wire or two opposite contrast slightly offset from the center, depending on the orientation of the easy c-axis and hence the magnetization relative to the tip magnetization. The competing anisotropy contribution manifest in relatively low switching fields of between 30 mT and 160 mT. In the case of the orthogonal anisotropy present in this case the angle dependence of the switching fields is not as trivial as for α-Fe.

The artificial nanowires were tailored by an EBL/metal deposition process with the aim to create Ising spin simulating single domain magnets. Such bars would feature a polar contrast at the ends, and patterns thereof also at sites of frustration. Three types of patterns with increasing scale were realized. Firstly, bars arranged in a growing number of triple junctions. The MFM studies reveal the expected magnetization arrangements for the zero field case. Upon applying an out of plane field some of the elements switch in a way indicating a strong in-plane component as would be caused by a tilted sample. One such pattern featured a break down of the shape anisotropy dominated magnetization arrangement at the kink between two elements. Secondly, hexagons set in patterns of rising size and complexity. Here contrast was found aside of that expected at the triple junctions as well as rearranging magnetizations to align with the in-plane component of the applied field. Lastly, a very large square lattice where the focus was placed on the edge effects. For the last type it was found that the elements in each row or column are always magnetized head to tail, meaning that the state of an entire row or column can be read out from the state of the according edge triple junction. Also the contrast across the quadruple junctions indicates the magnetization direction of the crossing row and column. All the switching taking place occurred in the rows which again indicates an in-plane component of the applied field of sufficient strength to cause switching.

The results highlight the fact that the interplay of anisotropies dominates the resulting remanent magnetization states in magnetic nanowires. Detailed information on the actual structure and defects is required order to comprehend the actual magnetic configuration and switching effects. The strength of hr-MFM set up was demonstrated by delivering results from various types of samples. Especially the ability to simultaneously observe the magnetization arrangement of a multitude of nanomagnets makes it a valuable tool. The magnetic tip can cause switching, an effect which in theory could be harnessed to manipulate individual nanomagnets. Use of special low moment high resolution tips enabled the observation of weak signals and minimized perturbations caused by the tip. Particular importance is placed on the results on the transverse magnetization of iron carbide nanowires which have not reported previously. Also the switching field results and rough angle dependence were first measured by the author. The results at hand underline that single domain magnets are a great toolkit which can be applied to investigate several fundamental and applied concepts.

References

[1] Parkin S S P, Hayashi M, and Thomas L 2008 *Science* **320** 190 7

[2] Cowburn R P, and Welland M E 2000 *Science* **287** 1466 7

[3] Wang R F, Nisoli C, Freitas R S, Li J, McConville W, Cooley B J, Lund M S, Samarth N, Leighton C, Crespi V H, and P Schiffer 2006 *Nature* **439** 303 7, 67

[4] Klingeler R, Hampel S, and Büchner B 2008 *Int. J. Hyper-thermia* **24** 496-505 7

[5] Castelnovo C, Mössner R, and Sondhi S L 2008 *Nature* **451**, 42 8, 25

[6] Iijima S 1991 *Nature* **354** 56-58 10

[7] Lu X, and Chen Z 2005 *Chemical Reviews* **105** (10) 36433696. 10

[8] Kataura H, Kumazawa Y, Maniwa Y, Umezu I, Suzuki S, Ohtsuka Y, and Achiba Y 1999 *Synthetic Metals* **103** (13) 25552558 10

[9] Yu M, Lourie O, Dyer M J, Kelly T F, and Rouff R D 2000 *Science* **287** 5453 11

[10] Demczyk B G, Wang Y M, Cumings J, Hetman M, Han W, Zettl A, and Ritchie R O 2002 *Mater. Sci. Eng. A* **334** 173-178 11, 56

[11] Yu M, Kowalewski T, and Ruoff R S 2000 *Physical Review Letters* **85** 1456 11

[12] Lipert K, Kretzschmar F, Ritschel M, Leonhardt A, Klingeler R and Büchner B 2009 *J. Appl. Phys.* **105** 063906 11

[13] Keithley J F 1999 "The Story of Electrical and Magnetic Measurements: From 500 B.C. to the 1940s" Wiley-IEEE Press 12

[14] Wasilewski P, Günther K 1999 *Geophysical Research Letters* **26** (15) 2275 78 12

[15] Myers H P 1997 "Introductory Solid State Physics" Crc Press Inc 13

[16] Chikazumi S 1997 "Physics of Ferromagnetism" Oxford Universtiy Press 14

[17] Skomski R 2007 "Simple models of Magnetism" Oxford University Press 18, 21

[18] Hubert A and Schäfer R 1998 "Magnetic Domains" Springer 21

[19] Wernsdorfer W, Bonet Orozco E, Hasselbach K, Benoit A, Barbara B, Demoncy N, Loiseau A, Pascard H, and Mailly D 1997 *Phys. Rev. Lett.* **78** 17911794 23

[20] Häglund J, Grimvall G, and Jarlborg T 1991 *Phys. Rev. B* **44**, 2914 23

[21] Arzhnikov A K, Dobysheva L V, and Demangeat C 2007 *J. Phys.: Condens. Matter* **19** 196214 23, 24

[22] Hofer L J E and Cohn E M 1957 *J. Am. Chem. Soc.* **81**, 1576 23

[23] Shabanova I N and Trapeznikov V A 1973 *Pis'ma Zh. Eksp. Teor. Fiz.* **18** 576 23

[24] Duman E, Acet M, Wassermann E F, Itie J P, Baudelet F, Mathon O, and Pascarellli S

2005 *Phys. Rev. Lett.* **94** 075502 24

[25] Jiang C, Srinivasan S G, Caro A, and Maloy S A 2008 *J. Appl. Phys.* **103**, 043502 24, 56

[26] Blum P, and Pauthenet R 1957 *Compt. Rend* **273** 1501 24, 57

[27] Harris M J, Bramwell S T, McMorrow D F, Zeiske T, and Godfrey K W 1997 *Phys. Rev. Lett* **79**, 2554-2557 25

[28] Gingras M J P 2009 *Science* **326**, 375 25

[29] Dirac P A M 1931 *Proceedings of the Royal Society* **A133** 6072. 25

[30] Aoki H, Sakakibara T, Matsuhira K, and Hiroi Z 2004 *J. Phys. Soc. Jpn* **73**, 2851-2856 25

[31] Higashinaka R, Fukazawa H, Deguchi K, and Maeno Y 2004 *J. Phys. Soc. Jpn* **73**, 2845-2850 25

[32] Binnig G, Rohrer H, Gerber C, and Weibel E 1982 *Phys. Rev. Lett.* **49** (1) 57-61 28

[33] Binnig G, Quate C F, and Gerber C 1986 *Phys. Rev. Lett. 56* (9) 930-933 28

[34] Nonnenmacher N, O'Boyle M P, and Wickramasinghe H K 1991 *Appl. Phys. Lett.* **58** 2921 29

[35] Saenz J J, Garcia N, Grütter P, Meyer E, Heinzelmann H, Wiesendanger R, Rosenthaler L, Hidber H R, and Güntherodt H J 1987 *J. Appl. Phys.*, **62(10)** 4293 31

[36] Martin Y, and Wickramasinghe H K 1987 *Appl. Phys. Lett.* **50** (20) 1455-1457 31

[37] Hartman U 1989 *Phys. Lett. A* **137** 475 32

[38] Wolny F, Weissker U, Mühl T, Leonhardt A, Menzel S, Winkler A, and Büchner B 2008 *J. App. Phys.* **104** 064908 33

[39] Müller C, Elefant D, Leonhardt A, and Büchner B 2008 *J. Appl. Phys.* **103** 034302 39, 42, 46, 50

[40] Hampel S, Kunze D, Haase D, Krämer K, Rauschenbach M, Ritschel M, Leonhardt A, Thomas J, Oswald J, Hoffmann V, and Büchner B 2008 *Nanomedicine* **3** 175 39

[41] Costa S, Borowiak-Palen E, Bachmatiuk A, Rümmeli M H, Gemming T, and Kalenczuk R J 2007 *Physica Status Solidi. B* **244** 4315-4318 39

[42] Weissker U, Löffler M, Wolny F, Lutz M U, Scheerbaum N, Klingeler R, Gemming T, Mühl T, Leonhardt A, and Büchner B 2009 *J. Appl. Phys.* **106** 054909 39, 54, 55

[43] Wang W, Wang K, Lv R, Wei J, Zhang X, Kang F, Chang J, Shu Q, Wang Y, and Wu D 2007 *Carbon* **45**, 1127-1129 39

[44] Lutz M U, Weissker U, Wolny F, Müller C, Löffler M, Mühl T, Leonhardt A, Klingeler R, and Büchner B 2010 *J. Phys.: Conf. Ser.* **200** 072062 46, 50, 51, 52, 54, 58, 59

[45] Löffler M, Weissker U, Mühl T, Gemming T, Eckert J, and Büchner B 2011 *Adv. Mater.* **23** 541-544 46

[46] Lipert K, Bahr S, Wolny F, Atkinson P, Weißker U, Mühl T, Schmidt O, Büchner B, and Klingeler R 2010 *Appl. Phys. Lett.* **97** 212503 49, 53

[47] Sorop T G, Untiedt C, Luis F, Kröll M, Rasa M, and de Jongh L J 2003 *Phys. Rev. B* **67**, 014402 51

[48] McVitie S, Ferrier R P, Scott J, White G S, and Gallagher A 2001 *J. Appl. Phys.* **89** 3656 53

[49] Skomski R, Zeng H, Zheng M, and Sellmyer D J 2000 *Phys. Rev. B* **62**, 3900 53

[50] Wernsdorfer W, Doudin B, Mailly D, Hasselbach K, Benoit A, Meier J, Ansermet J P, Barbara B 1996 *Phys. Rev. Lett.* **77** 1873 53

[51] Banerjee P, Wolny F, Pelekhov D V, Herman M R, Fong K C, Weissker U, Mühl T, Obukhov Y, Leonhardt A, Büchner B, and Hammel C P 2010 *Apl. Phys. Lett.* **96** 252505 53

[52] Silva E L, Nunes W C, Knobel M, Denardin J C, Zanchet D, Pirota K, Navas D, and Vazquez M 2006 *Physica B: Condensed Matter* **384** 22 54

[53] Belliard L, Milat J, Thiavelle A, Dubois S, Duvail J L, and Piraux L 1998 *J. Magn. Magn. Mat.* **190**, 1-16 54

[54] Seki I and Nagata K 2005 *ISIJ Int.* **45** 1789-1794 55

[55] Yu M, Lourie O, Dyer M J, Kelly T F, and Rouff R D 2000 *Science* **287** 5453 56

[56] Löffler M unpublished data 64

[57] Möller G and Mössner R 2006 *PRL* **96** 237202 67

List of Publications

1. Weissker U, Löffler M, Wolny F, **Lutz M U**, Scheerbaum N, Klingeler R, Gemming T, Mühl T, Leonhardt A, and Büchner B 2009 "Perpendicular magnetization of long iron carbide nanowires inside carbon nanotubes due to magnetocrystalline anisotropy" *J. Appl. Phys.* **106** 054909

2. **Lutz M U**, Weissker U, Wolny F, Müller C, Löffler M, Mühl T, Leonhardt A, Klingeler R, and Büchner B 2010 "Magnetic properties of a-Fe and Fe3C nanowires" *J. Phys.: Conf. Ser.* **200** 072062

3. Schulze C, Faustini M, Lee J, Schletter H, **Lutz M U**, Krone P, Gass M, Sade K, Bleloch A L, Hietschold M, Fuger M, Suess D, Fidler J, Wolff U, Neu V, Grosso D, Makarov D and Albrecht M 2010 "Magnetic films on nanoperforated templates: a route towards percolated perpendicular media" *Nanotechnology* **21** 495701

4. **Lutz M U**, Lipert K, Krupskaya Y, Bahr S, Wolter A, El-Gendy A A, Hampel S, Leonhardt A, Taylor A, Krämer K, Büchner B, Klingeler R "Feasibility of magnetically functionalised carbon nanotubes for biological applications: from fundamental properties of individual nanomagnets to nanoscaled heaters and temperature sensors" in: R. Klingeler, R.B. Sim: "Carbon Nanotubes for Biomedical Applications" Springer 2011, p. 97-124

Danksagung

Ich möchte allen danken, die mich auf meinem Weg unterstützt haben.

Den Kollegen in Dresden für Zusammenarbeit, wissenschaftlichen Austausch und für eine gute Zeit. Allen voran Thomas Mühl, der mich wie ein zweiter Betreuer ständig begleitet hat. Weiters Franziska Wolny, Uhland Weissker und Markus Löffler mit denen ich viele Stunden vor Mikroskopen aller Art und in Diskussionen verbracht habe. Meinen Bürokollegen Kamil Lipert, Yulia Krupskaya und Ahmed El Gendy für eine angenehme Atmosphäre. Last but certainly not least Prof. Rüdiger Klingeler, dessen Tür immer für mich offen stand und der alles ermöglicht hat.

In Wien will ich meinen Eltern Wolfgang und Johanna danken, speziell für die Unterstützung während des Masterstudiums und für die erneute Beherbergung nach meiner Rückkehr aus Dresden. Meinem Bruder Basti für Verständnis und Ablenkung. Meiner Großmutter Waltraud für die Bereitstellung eines Arbeitsplatzes und eine vorzügliche Bewirtung. Meiner Tante Claudia für Korrekturen und moralische Unterstützung. Allen Verwandten und Freunden, die mir mit Rat und Tat zur Seite standen.

Meinen Hunden Micha und Luky, die mich bei Eingebung suchenden Spaziergängen begleitet haben. Gogi der Schildkröte, für die ich in Pausen immer gerne Löwenzahn gepflückt habe. Alice für alles.

Erklärung gemäß § 8 (3) b) der Promotionsordnung

Ich erkläre hiermit, dass ich die vorgelegte Dissertation selbst verfasst und mich dabei keiner anderen als der von mir ausdrücklich bezeichneten Quellen und Hilfen bedient habe.

Wien, am 14. Mai 2012

Matthias Uljas Lutz